Materials Physics Laboratory

Espoo 2001

DYNAMICAL PROPERTIES OF SINGLE-ELECTRON DEVICES AND MOLECULAR MAGNETS

Teemu Pohjola

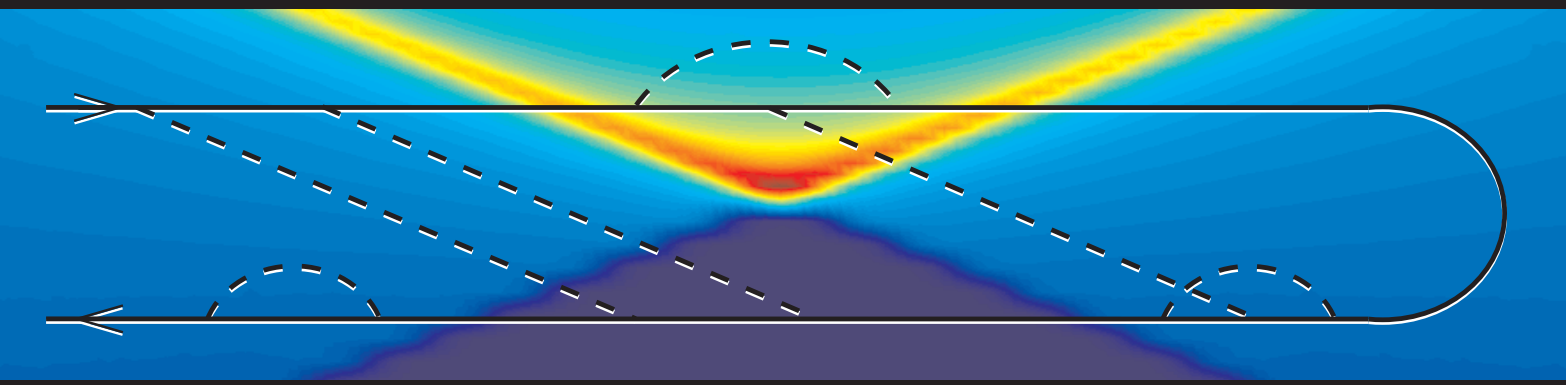

TEKNILLINEN KORKEAKOULU
TEKNISKA HÖGSKOLAN
HELSINKI UNIVERSITY OF TECHNOLOGY
TECHNISCHE UNIVERSITÄT HELSINKI
UNIVERSITE DE TECHNOLOGIE D´HELSINKI

Helsinki University of Technology Publications in Engineering Physics
Teknillisen korkeakoulun teknillisen fysiikan julkaisuja
Espoo 2001 TKK-F-A805

DYNAMICAL PROPERTIES OF SINGLE-ELECTRON DEVICES AND MOLECULAR MAGNETS

Teemu Pohjola

Dissertation for the degree of Doctor of Science in Technology to be presented with due permission of the Department of Engineering Physics and Mathematics for public examination and debate in Auditorium F1 at Helsinki University of Technology (Espoo, Finland) on the 10th of February, 2001, at 12 o´clock noon.

Helsinki University of Technology
Department of Engineering Physics and Mathematics
Materials Physics Laboratory

Teknillinen korkeakoulu
Teknillisen fysiikan ja matematiikan osasto
Materiaalifysiikan laboratorio

Distribution:
Helsinki University of Technology
Materials Physics Laboratory
P.O. Box 2200
FIN-02015 HUT
Tel. +358-9-451 3150
Fax. +358-9-451 3164
E-mail: teemu.pohjola@hut.fi

ISBN 951-22-5324-0
ISSN 1456-3320

Otamedia Oy
Espoo 2001

Preface

This work has been carried out in the Materials Physics Laboratory at the Helsinki University of Technology and in the Institute for Theoretical Solid State Physics at the University of Karlsruhe, Germany.

I would like to express my deep gratitude to Gerd Schön and Herbert Schoeller for initiating me into this exciting field of physics. I greatly appreciate their insightful advice and hearty encouragement throughout my research work. I am also indebted to all the other co-authors in the contributed Papers – Daniel Boese, Jürgen König, Martti Salomaa, and Jörg Schmid – for the fruitful collaboration and the good times in the past four years. Martti Salomaa, the supervisor of this Thesis, is further acknowledged for his invaluable support and the excellent working conditions provided in the Materials Physics Laboratory. The assistance from Tero Heikkilä during the final stages of writing is greatly appreciated together with his companionship through these years.

I am much obliged to the collaboration and enlightening discussions with the experimental groups of Pertti Hakonen in Espoo, Leo Kouwenhoven in Delft, Jukka Pekola in Jyväskylä, Myriam Sarachik in New York, Jürgen Weis at the Max Planck Institut in Stuttgart, and Wolfgang Wernsdorfer in Grenoble. In addition, the theoretical collaboration with Michael Leuenberger and Daniel Loss is gratefully acknowledged.

All my collagues and friends deserve my wholehearted thanks for the invigorating atmosphere at work and the relaxing leisure. In addition to those already mentioned, I wish to thank especially the following people for the jolly good times: Jouni Knuuttila, Julius Koskela, Saku Lehtonen, Tapani Makkonen, Jussi Perkiö, Janne Salo, Sami Virtanen, and Pekka Äyräs; and Wolfgang Belzig, Fabian Braun, Michele Governale, Ziv Hermon, Thomas Schauerte, Alexander Schnirman, Karl-Heinz Wagenblast, Frank Wilhelm, and all the flat mates I had in Kapellenstrasse 66. The secretarial help from Orvokki Nyberg, Tamriko Samsonadze, Roswitha Schrempp, and Evmarie Schwartz is also greatly appreciated.

Personal scholarships from the Finnish Academy of Science and Letters and the Finnish Cultural Foundation are gratefully acknowledged. I am also indebted to the Academy of Finland, the Deutsche Akademische Austauschdienst (DAAD) and the "Dynamics of Nanostructures" program of the European Union for their financial support. The Center for Scientific Computing (CSC) is acknowledged for providing excellent computing resources.

Finally, I would like to thank my family for their support and my dear spouse Riikka for her loving patience and encouragement in the course of this work.

Espoo, October, 2000

Teemu Pohjola

List of Publications

This thesis is a review of the author's work in the fields of single-electron devices and molecular magnets. It consists of an overview and the following selection of the author's publications in these fields:

I. Teemu Pohjola, Jürgen König, Herbert Schoeller, and Gerd Schön, *Strong Tunneling in Double-Island Structures*, Physical Review B**59**, 7579 (1999).

II. Teemu Pohjola, Jürgen König, Martti Salomaa, Jörg Schmid, Herbert Schoeller, and Gerd Schön, *Resonant Tunneling through a Two-Level Dot and Double Quantum Dots*, Europhysics Letters **40**, 189 (1997).

III. Teemu Pohjola, Daniel Boese, Jürgen König, Herbert Schoeller, and Gerd Schön, *Strong Tunneling in Small Quantum Dots: Kondo Effect in Two Model Systems*, Journal of Low Temperature Physics **118**, 391 (2000).

IV. Teemu Pohjola, Herbert Schoeller, and Gerd Schön, *Orbital and Spin Kondo Effects in a Double Quantum Dot*, HUT Report Series, TKK-F-A802 (submitted for publication).

V. Jürgen König, Teemu Pohjola, Herbert Schoeller, and Gerd Schön, *Transport through Quantum Dots and the Kondo Problem*, invited contribution to the Proceedings of the NATO ASI "Quantum Mesoscopic Phenomena and Mesoscopic Devices in Microelectronics", Eds. I.O. Kulik and R. Ellialtioglu, Kluwer Academic Publishers, Dordrecht, NATO Science Series C, vol. **559**, pp. 161-167 (2000).

VI. Teemu Pohjola and Herbert Schoeller, *Spin Dynamics of Mn_{12}-acetate in the Thermally-Activated Tunneling Regime: ac-Susceptibility and Magnetization Relaxation*, Physical Review B **62**, 15026 (2000).

Throughout the overview, the above mentioned papers are referred to by their Roman numerals.

Author's Contribution

The research reported in this Thesis has been carried out during the years 1996-2000 in the Materials Physics Laboratory at the Helsinki University of Technology and in the Institute for Theoretical Solid State Physics at the University of Karlsruhe, Germany.

The author has contributed extensively to all aspects of the research work reported in this Thesis. In Papers I-IV and VI, the theoretical formulation of the problems as well as the analytical and numerical calculations presented were carried out by the author. He also devised several computer programs and numerical algorithms used in these papers. In Paper V, the author was responsible for the calculations regarding the double-dot and two-level dot models.

The author has also actively participated in the reporting of the research work presented in this Thesis. Papers I-IV and VI were primarily written by the author and he has presented the work at several international conferences.

Contents

1 Introduction

On the microscopic scale of atoms and molecules, all physical systems are characterized by discrete *quantized* states. However, the units of quantization are so minute that the macroscopic world around us is usually perceived as continuous, and the number of particles is so large that macroscopic systems obey the laws of *classical* mechanics and electrodynamics. Between these extremes, there exists an intermediate or *mesoscopic* regime, where condensed-matter systems can exhibit quantum mechanical behaviour in the normal non-condensed state.

The motivation for research on mesoscopic physics is twofold. Firstly, the miniaturization of components for microelectronics is rapidly approaching the limit where quantum mechanical effects become important, and conventional device design concepts seize to function properly. Secondly, recent advances in nanofabrication technologies have opened a range of new experimental possibilities: semiconductor heterostructures can be grown with the precision of atomic monolayers [1]; structures can be patterned with lithography down to linewidths of 10–20 nm and below [2]; metal grains a few nanometers in size [3–6] and even single molecules [7] can be integrated into electric circuits. In these examples, the motion of the conduction electrons is confined in one or more directions, and effective two-, one-, and even zero-dimensional structures are accomplished. Consequently, the electronic states are quantized in the direction(s) of the confining potential. These kinds of low-dimensional structures are of fundamental interest in that they enable tunable realizations of various quantum mechanical models.

The central ideas in this Thesis can be illustrated in terms of a tiny normal-metal or magnetic grain coupled to an external measurement apparatus. Let us first consider a normal-metal grain coupled to a pair of electric leads via tunnel junctions – Fig. 1 shows one possible experimental setup employed for this purpose.

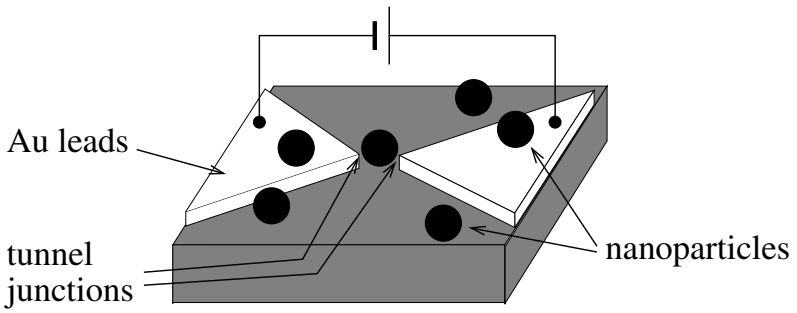

Figure 1: Schematic of the device used in Ref. [6] to study electron transport through CdSe nanoparticles having a diameter of 5.5 nm.

For decreasing size of the grain, the strong on-site Coulomb interaction between the electrons is enforced. This increases the energy required for changing the number of electrons in the grain and, hence, that for the electrons to tunnel in or out of the grain. In sufficiently small grains, this *charging energy* exceeds the available excitation energies:

the thermal energy $k_{\rm B}T$ and the bias voltage eV applied between the electrodes. As a consequence, the number of electrons in the grain becomes fixed and the tunneling current through the grain is suppressed. This phenomenon is known as the *Coulomb blockade* effect [8–12] and it forms the basis for the so-called single-electron devices. The charging energy varies inversely proportionally to the grain surface area and the charging effects have been observed in single atoms [7] and ultrasmall grains [5] even up to room temperature.

In ultrasmall metal grains, the level spacing between the single-electron quantum states is large and may exceed the thermal energy $k_{\rm B}T$. The tunneling current can only traverse the grain via the available states and hence it directly reflects the discrete electronic spectrum. This has been observed for metal particles of diameters < 10 nm [3–6]. Structures displaying a discrete spectrum are denoted *artificial atoms*, owing to their resemblance with the electronic states in real atoms.

In magnetic grains, the magnetization is composed of a large number of atomic spins and angular momenta. In ultrasmall grains – with diameters below 10 nm – also the magnetization becomes quantized and starts to behave as a single giant spin; nanoparticles with magnetic moments $90 - 6000\ \mu_{\rm B}$ have been studied experimentally [13]. Recently, yet smaller magnetic structures have been realized: certain synthetic materials are composed of identical magnetic molecules having spins $S \leq 10$ [14–17]. The smallness of the magnetic moment speeds up the process of magnetization reversal by enhancing the quantum mechanical tunneling of the magnetization. On the other hand, the discreteness of the spin states may hinder the tunneling, unless some pairs of states are at resonance. These phenomena are manifested as a magnetic-field dependent series of resonances in the measured relaxation rates [18–21].

The manipulation of the grains and their coupling to a macroscopic measurement device is difficult and in general is not suited for large-scale applications. At low temperatures, the quantization effects found in small grains can be realized in large structures specifically designed for this purpose. For example, while only extremely small grains exhibit charging effects at room temperature, lithographically fabricated metal structures with dimensions of order hundreds of nanometers are sufficient at sub-Kelvin temperatures. The larger size combined with convenient materials choices enables improved control and accuracy in the fabrication process and also makes these devices attractive for potential nanoelectronics applications.

In order to study and utilize these systems, they have to be coupled to a measuring device or at least attached to a sample holder. This coupling always involves exchange of particles (electrons) and/or heat between the structure under investigation and its surroundings. This is shown schematically in Fig. 2. The environment tends to disturb the smaller system and, depending on the type and strength of the coupling, the localized states acquire finite lifetimes, their coherent time evolution is perturbed, and the small system may be driven out of equilibrium. A detailed study of the coupling effects – in particular in the strong-coupling regime – is of fundamental physics as well as of

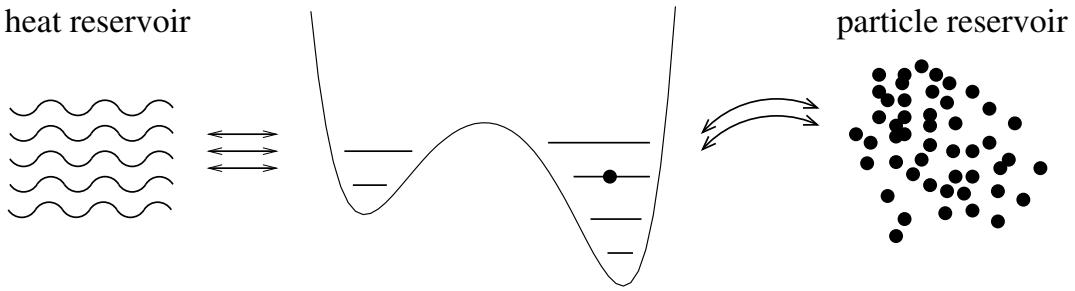

Figure 2: All the systems studied in this dissertation are realizations of the same class of models: a small system, possibly with internal dynamics (indicated by the double-well potential), is coupled to heat and/or particle reservoirs.

(nano)technological interest. This constitutes the subject of the present thesis.

Outline of the Thesis

This dissertation covers the author's work in the fields of single-electron devices and molecular magnets as presented in Papers I through VI. The overview of the thesis is organized in three parts; all parts are intended to be self-contained.

In the first part, single-electron devices based on lithographically fabricated metal structures (Paper I) and semiconductor heterostructures (Papers II-V) are introduced. In Section 2, charging effects and single-electron tunneling in these systems are discussed. The effects of quantum fluctuations on electron transport through metallic double-island structures (Paper I) and ultrasmall quantum dots (Papers II-V) are presented in Subsecs. 2.2 and 2.4, respectively.

In the second part, the magnetization dynamics in the molecular magnet Mn_{12}-acetate is reviewed (Paper VI). A microscopic model for the magnetic molecules and the rich quantum dynamics of the magnetization is discussed in Sec. 3. The results for arbitrary external magnetic fields are outlined in Subsec. 3.2 (Paper VI).

The third part of the thesis consists of a review of the theoretical methods employed in Papers I-VI. This order of presentation enables a self-contained account of the theory without interrupting the other sections. In Section 4, a single theoretical framework applicable to all the models considered is presented – each model consists of a small system with a discrete set of states coupled to heat and/or particle reservoirs. The full nonequilibrium dynamics of the discrete systems is described in terms of a recently developed diagrammatic technique [22–27].

This overview is concluded with a discussion of the results and the future prospects of single-electron devices and molecular magnets.

2 Single-Electron Devices

Single-electron devices (SED's) consist of one or more small electronic islands connected to each other and to a set of macroscopic electrodes via tunnel junctions. While the tunnel junctions enable the transport of electrons through the system, the onsite Coulomb repulsion may suppress the current by inhibiting any changes in the number of electrons on the islands. In SED's, one exploits these properties: electron transport is strongly influenced by the discreteness of the electric charge and can be manipulated at the level of single electrons [10–12].

In Papers I-V, we consider the electronic islands in two limits: first, with a continuous single-particle spectrum and, second, with a discrete spectrum and a large level spacing. These are realized in metallic and semiconductor devices, respectively. In Subsec. 2.1, we first introduce the Coulomb-blockade effects in the context of single and double metal islands. The additional features arising from the discrete spectrum in semiconductor quantum dots are the subject of Subsec. 2.3.

The tunneling coupling between the islands and the adjacent electrodes leads to quantum fluctuations of the charge and, in small quantum dots, also of the spin degree of freedom. Section 2.2 summarizes the main results of strong tunneling in a system of two metal islands between macroscopic leads. Strong tunneling in small single and double quantum dots is studied in Papers II-V and the results obtained are summarized in Subsec. 2.4.

2.1 Metal Islands

The Coulomb-blockade effects are best illustrated in terms of metal structures owing to two characteristic properties of metals: 1) due to the efficient screening of electric potentials, the Coulomb interactions between electrons are well described by the classical electrostatic charging energy [10,11]; and 2) due to the continuous spectrum of electronic states, the state of the island is fully determined by just two quantities: the charge and the electrochemical potential. Metallic single-electron devices are typically fabricated using shadow evaporation techniques [11]; the tunnel junctions are formed between metal stripes when their connecting surfaces are let oxidize, see Fig. 3a. The islands may be more than one micron long and a typical junction has an area of 100 nm $\times$ 100 nm and a capacitance of $\sim 10^{-15}$ F.

Coulomb-Blockade Effects

Let us illustrate the effect of the charging energy, $E_{\rm ch}(n;n_x)$, on electron transport in the model system known as the *single-electron transistor* (SET), see Fig. 3b. For n excess electrons on the central island (added to a neutral configuration of n_0 electrons and the positive background charge $n_0 e$),

$$E_{\rm ch}(n;n_x) = E_C(n-n_x)^2. \tag{1}$$

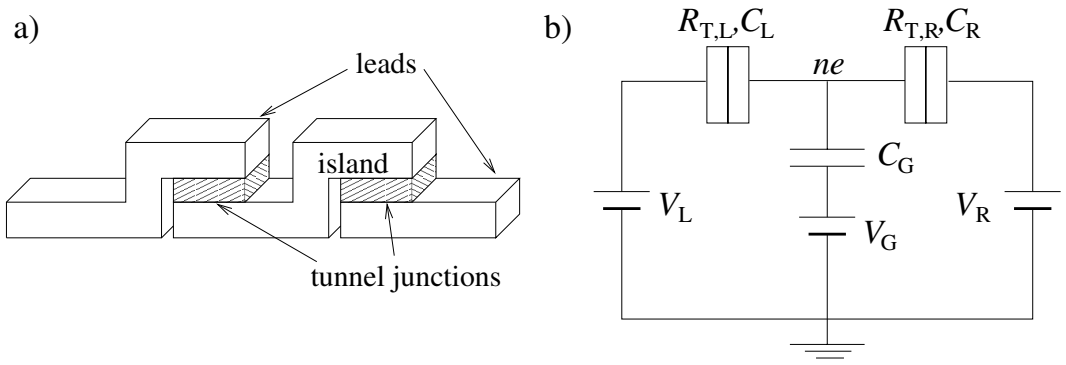

Figure 3: a) Typical fabrication scheme for a metallic single-electron transistor. b) Equivalent electric circuit of a SET with n electrons on the central island; the C's denote capacitances, V's voltages, and R_T tunneling resistances.

Here $en_x = C_L V_L + C_R V_R + C_G V_G$ is the total external charge at the junctions and on the gate capacitor; the capacitances and voltages follow the notation of Fig. 3b. Figure 4a shows the charging energy as a function of the gate charge n_x for the charge states $n = -2, ..., 3$. Due to the periodicity of $E_{ch}(n; n_x)$, it suffices to consider only the regime $0 \leq n_x \leq 1$, where the states $n = 0, 1$ have the lowest energy. The energy scale for single-electron charging effects is determined by the prefactor in Eq. (1): $E_C = e^2/2C$ with $C = C_L + C_R + C_G$ being the total capacitance of the island. For a typical junction, $E_C \sim 1$ K, while experimental temperatures can be routinely extended down to 50–100 mK.

Transport of electrons through the island is only possible if the number of the electrons on the island, n, can be changed. This requires energy and, in the region around the circled crossing in Fig. 4a, the relevant excitation energy is given by $\Delta_0 \equiv E_{ch}(1) - E_{ch}(0)$ (here and in what follows, the n_x dependence of $E_{ch}(n) = E_{ch}(n; n_x)$ is implicitly assumed). Away from the resonance at $n_x = 0.5$, we have $\Delta_0 \neq 0$ and the available excitation energies may be inadequate for changing n, i.e., $k_B T, eV \ll |\Delta_0|$. In this case, the system resides in its ground state with n fixed to either 0 or 1. The consequent suppression of the current is known as Coulomb blockade. Since Δ_0 depends on n_x, the linear conductance G displays oscillations as a function of the gate voltage, see Fig. 4b. This was first measured in Ref. [9]. The single-electron transistor owes its name to this high sensitivity of the current on the gate voltage/charge and it has found applications in, e.g., electrometers [11, 28–30].

Figure 5a presents another way of visualizing the SET. In the figure, two tunnel barriers separate the island from the leads; the chemical potentials in the leads, $\mu_r = -eV_r$, and the addition energy Δ_0 (Δ_1) for the first (second) electron added to the island are also shown. The transport of electrons takes place as a sequence of single-electron tunneling processes (denoted by the solid arrow in the figure). If initially $n = 0$, an electron can tunnel into the island from the left lead provided that $\mu_L > \Delta_0$. The tunneling of a second electron (dashed arrow) is forbidden for $\mu_L < \Delta_1$ and one electron first has to

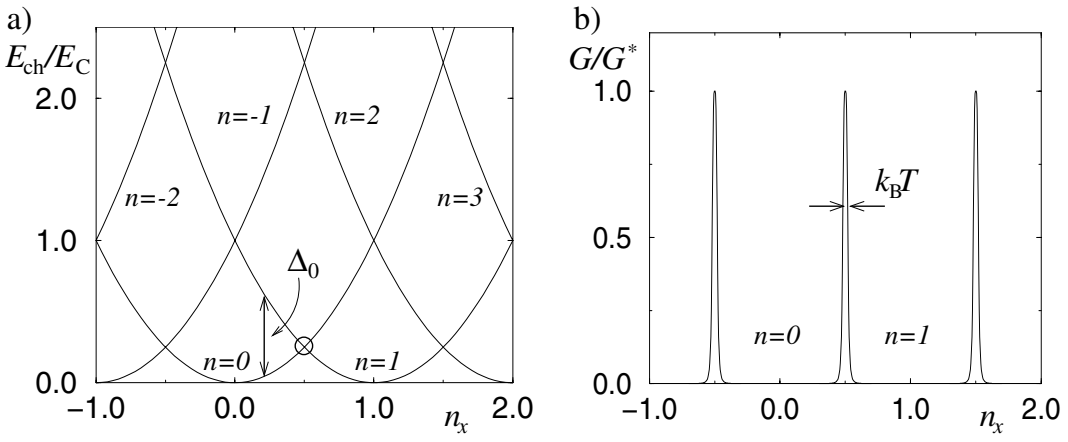

Figure 4: a) Charging energy $E_{\rm ch}(n)$ as a function of the gate charge n_x for the charge states $n = -2, ..., 3$. At low temperatures and for $0 < n_x < 1$, the charge states $n = 0, 1$ dominate electronic transport; the relevant excitation energy is $\Delta_0 = E_{\rm ch}(1) - E_{\rm ch}(0)$. b) Coulomb oscillations of the linear conductance G as a function of n_x. The orthodox theory yields conductance peaks with constant height and a thermal broadening. The charge n acquires a well-defined integer value between the current peaks.

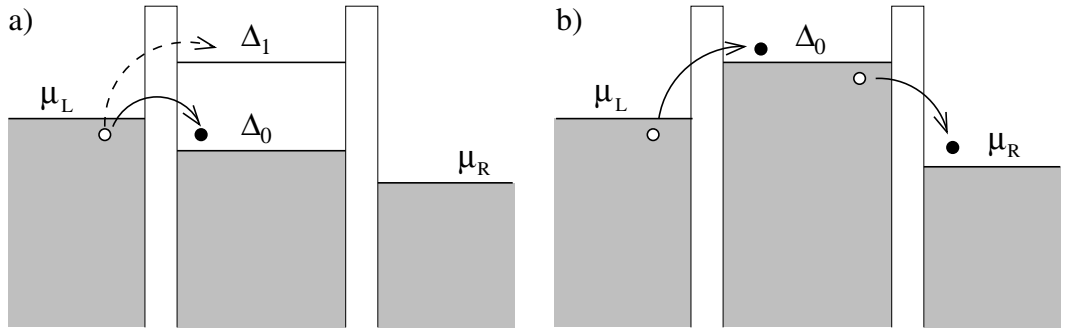

Figure 5: Energy representation of a single-electron transistor: a metal island separated by tunnel barriers from two metal leads (the gray continua denote the continuous spectra). The levels denote the addition energies Δ_n of the nth electron. a) The solid and dashed arrows denote energetically allowed and forbidden tunneling processes, respectively. b) In a second-order or *cotunneling* process, two electrons can tunnel in a single coherent process transferring one electron from the left to the right lead.

leave the island – this is possible if the consequent change in the energy, Δ_0, exceeds $\mu_{\rm R}$. Combining these restrictions leads to the condition $\mu_{\rm L} > \Delta_0 > \mu_{\rm R}$ for the current to flow at low temperatures.

In order to provide a more quantitative account of the Coulomb-blockade effects, let us consider the occupation probabilities of the charge states, p_0 and p_1 ($p_0 + p_1 = 1$). These are governed by the master equations

$$\frac{\partial p_0(t)}{\partial t} = \sum_r \left[p_1(t)\Sigma^r_{1\to 0} - p_0(t)\Sigma^r_{0\to 1}\right] \tag{2}$$

$$\frac{\partial p_1(t)}{\partial t} = \sum_r \left[p_0(t)\Sigma^r_{0\to 1} - p_1(t)\Sigma^r_{1\to 0}\right], \tag{3}$$

where $\Sigma^r_{n\to n\pm 1}$ is the rate for tunneling into and out of the island through junction r (here the rates are assumed time independent). The classical rates [10] are given by $\Sigma^r_{n\to n\pm 1} = 2\pi\alpha^{\pm}_r(\Delta_n)$ with

$$\alpha^{\pm}_r(\omega) = \pm\alpha^r_0 \frac{\omega - eV_r}{\exp[\pm\beta(\omega - eV_r)] - 1}. \tag{4}$$

Here $\beta = 1/k_{\rm B}T$ and $\alpha^r_0 \equiv R_{\rm K}/(4\pi^2 R_{{\rm T}r})$ is the dimensionless conductance of the junction; $R_{{\rm T}r}$ is the tunneling resistance and $R_{\rm K} = h/e^2$ is the quantum of resistance. In the stationary state, $p_i(t) = p_i$, the current from the left to the right lead is attained from the same probabilities and rates as

$$I = I_{\rm R} = -e\left[p_0\Sigma^{\rm R}_{0\to 1} - p_1\Sigma^{\rm R}_{1\to 0}\right] = -2\pi e\left[p_0\alpha^+_R(\Delta_0) - p_1\alpha^-_{\rm R}(\Delta_0)\right] \tag{5}$$

(the current between the electrodes is conserved; hence $I = I_{\rm R} = -I_{\rm L}$). Note that the stationary state does not correspond to an equilibrium if $\mu_{\rm L} \neq \mu_{\rm R}$.

The simple approach outlined in this section is known as the *orthodox theory* of Coulomb blockade [10] and it explains, e.g., the Coulomb oscillations in Fig. 4b. It predicts the thermal broadening of the peaks and the constant peak height $G^* = \alpha^{\rm L}_0\alpha^{\rm R}_0/(\alpha^{\rm L}_0 + \alpha^{\rm R}_0)$ for the linear conductance at low temperatures.

Microscopic Model

For a more detailed description of the tunneling, let us define the Hamiltonian $\mathcal{H} = \mathcal{H}_0 + \mathcal{H}_{\rm T}$, where $\mathcal{H}_0 = \mathcal{H}_{\rm L} + \mathcal{H}_{\rm R} + \mathcal{H}_{\rm I}$ individually describes the left and right reservoirs and the island, while $\mathcal{H}_{\rm T}$ accounts for the tunneling coupling. More specifically,

$$\mathcal{H}_r = \sum_{km} \varepsilon_{rkm} c^\dagger_{rkm} c_{rkm} \quad \text{for} \quad r = {\rm L}, {\rm R}, \tag{6}$$

$$\mathcal{H}_{\rm I} = \sum_{qm} \varepsilon_{qm} c^\dagger_{qm} c_{qm} + E_{\rm C}(\hat{n} - n_x)^2, \tag{7}$$

$$\mathcal{H}_{\rm T} = \sum_{rkqm} (T^{rm}_{kq} c^\dagger_{rkm} c_{qm} e^{-i\hat{\phi}} + H.c.), \tag{8}$$

where k and q denote the wave vectors in the leads and on the island, respectively, m is the transverse channel number (including the spin) which is conserved in the tunneling, and $\hat{n} = \sum_{qm} c^\dagger_{qm} c_{qm}$. The operator $e^{\pm i\hat{\phi}}$ changes the charge on the island by $\pm e$. Here it is assumed that the charge and the fermionic degrees of freedom can be considered separately because of the large number of electrons on the metal island. The tunneling matrix elements T^{rm} ($T^{rm} = T^{rm}_{kq}$ is assumed to be independent of the wave vectors) are related to the tunneling resistance through

$$\frac{1}{R_{\mathrm{T}r}} = \frac{2\pi e^2}{\hbar} \sum_m N^m_r(0) N^m_{\mathrm{I}}(0) |T^{rm}|^2, \tag{9}$$

where $N^n_{r(\mathrm{I})}(0)$ denote the densities of states in the leads (island).

Double-Island Structures

The single-electron transistor model is readily generalized to a system of two islands, see Fig. 6a. This system has been extensively studied in Refs. [31–39] and it is also the subject of Paper I. In this section, we discuss the additional features arising from the fact that the charge states are now given by two numbers (n_1, n_2) and can be manipulated with the two gate voltages $V_{\mathrm{G}i}$.

The charging energy may be defined such that the chemical potentials in the islands are zero, $\mu_1 = \mu_2 = 0$. It then takes the form

$$\begin{aligned} E_{\mathrm{ch}}(n_1, n_2) &= E_{\mathrm{CL}}(n_1 - n_{x1})^2 + E_{\mathrm{CR}}(n_2 - n_{x2})^2 \\ &+ E_{\mathrm{CM}}(n_1 - n_{x1})(n_2 - n_{x2}), \end{aligned} \tag{10}$$

where the prefactors depend on the various capacitances shown in Fig. 6a and define the energy scales for charge excitations. The gate charges $en_{x1} = V_{\mathrm{G}1}C_{\mathrm{G}1} + V_{\mathrm{L}}C_{\mathrm{L}}$ and $en_{x2} = V_{\mathrm{G}2}C_{\mathrm{G}2} + V_{\mathrm{R}}C_{\mathrm{R}}$ control the charge on the islands, see Fig. 6b. Due to the periodicity of the energy, it is sufficient to only consider gate voltages $0 \le n_{xi} \le 0.5$. In this interval, the tunneling of electrons is characterized by the states (0,0), (1,0), and (0,1), and the differences in the respective charging energies: $\Delta_{\mathrm{L}} \equiv E_{\mathrm{ch}}(1,0) - E_{\mathrm{ch}}(0,0)$, $\Delta_{\mathrm{R}} \equiv E_{\mathrm{ch}}(0,1) - E_{\mathrm{ch}}(0,0)$, and $\Delta_{\mathrm{M}} \equiv E_{\mathrm{ch}}(0,1) - E_{\mathrm{ch}}(1,0)$, see the encircled region in Fig. 6b. Below we denote Δ_b for charge transfer across the barrier $b = \mathrm{L}, \mathrm{M}, \mathrm{R}$.

Similar to the SET, the electric current through the double-island system is composed of a sequence of single-electron tunneling processes. Due to the strong intra and interdot Coulomb interactions, an electron cannot tunnel in from the left lead before the previous electron leaves the right island into the right lead. Because of this correlation effect, the current can only flow close to the nodes in Fig. 6b, rendering the rest of the plane the Coulomb-blockade regime. This effect provides the basis for a new kind of an application, the single-electron pump, that enables the transfer of electrons through the system one by one [11] (for an alternative way of achieving this, see Ref. [40]). This is accomplished by tuning the gate voltages in a cyclic fashion around a node, e.g., along the dashed oval in Fig. 6b. If the cycle is repeated with the frequency f, the current $I = ef$ is produced.

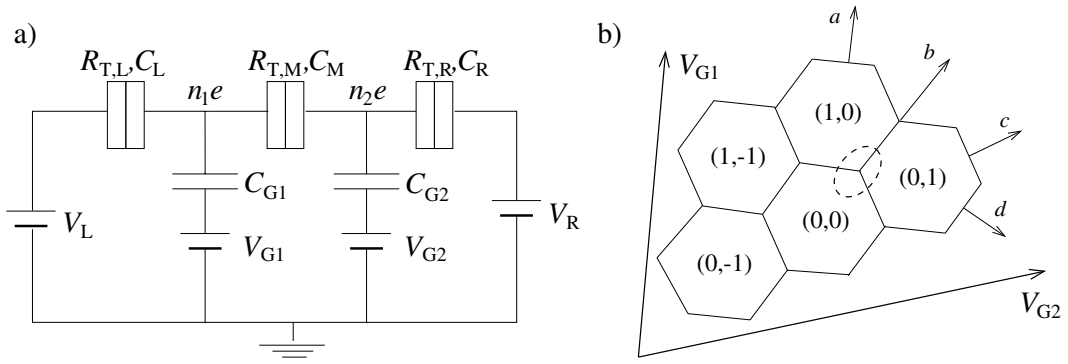

Figure 6: a) Schematic of a double-island structure considered in Paper I. b) The honeycomb in the (V_{G1}, V_{G2})-plane shows the regions where different charge configurations (n_1, n_2) minimize the charging energy. The arrow a (c) denotes the direction in which only n_1 (n_2) is changed. The total charge $n_1 + n_2$ remains constant in direction d. The special case, $V_{G1} = V_{G2}$, studied in Subsec. 2.2, corresponds to the direction of the arrow b.

Indeed, pumps based on long series of tunnel junctions are so accurate that they have been adopted in the definition of the new current standard [29, 41].

The tunneling rates and the microscopic Hamiltonian for more than a single island are straightforward generalizations of Eqs. (4)–(8) and, for the present system, are presented in detail in Paper I.

2.2 Strong Tunneling in Double-Island Structures

The simple picture of the metallic single-electron devices outlined in the previous subsection is sufficient in explaining the general features of the Coulomb-blockade effects in double-island structures. However, the orthodox theory, based on the lowest-order perturbation theory in the tunnel couplings, has turned out inadequate in explaining a number of recent experiments [31,32]. In several experimentally relevant regimes, higher-order tunneling processes contribute to the electron transport and give rise to quantum fluctuations of the charge on the island [34–39]. This leads to a nonvanishing current in the Coulomb-blockade regime and to strong modifications of the conductance peaks.

The quantum fluctuations in metal SED's have been considered, e.g., in Refs. [22–25, 36–39, 42–46] using an extensive range of theoretical approaches. The particular system consisting of two metallic islands (also large semiconductor quantum dots exhibit metallic properties) has been studied in Refs. [36–39]. In these works, the limiting cases $\alpha_0^{\rm M} \gg \alpha_0^{\rm L,R}$ and $\alpha_0^{\rm M} \ll \alpha_0^{\rm L,R}$ were considered. In Ref. [47], it was shown that the number of transverse channels in the junctions, N [indexed with m in Eq. (8)], becomes important already in second-order perturbation theory. Most of the previous work was focused on tunnel junctions with one or a few transverse channels, which is a realistic assumption for certain semiconductor quantum dots. In metal junctions, N is typically on the order

of 10^3 or more and quantum fluctuations lead to distinctly different behaviour.

In Paper I, we extend the previous approaches by allowing arbitrary relative magnitudes for the tunneling couplings and considering many-channel junctions, with $N \to \infty$, characteristic to metal SED's. We also present calculations applicable down to zero temperature and, on the other hand, up to tunneling conductances well in excess of the conductance quantum e^2/h, which is sometimes considered as the limit of validity for the tunneling Hamiltonian. This task is accomplished within the real-time diagrammatic approach introduced in Sec. 4 below. In this subsection, we summarize the main results obtained.

In what follows, let us consider left-right symmetry of the capacitances and tunneling conductances, and the special case of equal gate voltages/charges, $n_{x1} = n_{x2} = n_x$, corresponding to the direction b in Fig. 6b. In this case, $E_{\rm ch}(1,0) = E_{\rm ch}(0,1)$ and $\Delta_{\rm M} = 0$. Figure 7a displays the charging energy for the lowest charge states in the region $0 \le n_x \le 1$. The charging energy, Eq. (10), is characterized by two energy scales; the first scale

$$E_{\rm C} = \frac{\partial^2 E_{\rm ch}(n_1,n_2)}{\partial n_{xi}^2} = \frac{e^2}{2}\frac{1}{2(C+C_g)} \tag{11}$$

describes the overall charging of the double-island system and determines the curvature of the parabolas in Fig. 7a; the second energy scale

$$E_{\rm CM} = \frac{\partial^2 E_{\rm ch}(n_1,n_2)}{\partial n_{x1}\partial n_{x2}} = \frac{e^2}{2}\frac{2C_{\rm M}}{(C+C_g)(C+2C_{\rm M}+C_g)} \tag{12}$$

reflects the interisland Coulomb interaction and determines the energy cost for $n_1 \neq n_2$. In the weak-coupling limit, the conductance exhibits peaks at the degeneracy points marked by the vertical dashed lines in the figure. At low temperatures, the orthodox theory yields a series of peaks with constant height

$$G^* = \frac{2\pi}{3}\frac{e^2}{\hbar}\frac{\alpha_0^{\rm L}\alpha_0^{\rm M}\alpha_0^{\rm R}}{\alpha_0^{\rm L}\alpha_0^{\rm M}+\alpha_0^{\rm L}\alpha_0^{\rm R}+\alpha_0^{\rm M}\alpha_0^{\rm R}}. \tag{13}$$

The peak at n_x^* is shown in Fig. 7b for two temperatures (the solid curves). The conductance is rapidly suppressed when n_x is tuned off-resonant and Δ_b exceeds $k_{\rm B}T$. This leads to a thermal broadening of the peak.

Effects of Quantum Fluctuations

The probability for higher-order tunneling processes involving m electrons is proportional to $(\alpha_0^b)^m$. Therefore, an increasing coupling strength enhances their relative contribution to the current and conductance. The dimensionless conductances reflect the transparency of the barriers and, for $\alpha_0^b \to 1$, the islands essentially merge with the leads rendering the charge states (n_1,n_2) meaningless. However, for $\alpha_0^b \ll 1$, also the higher-order processes are well described in the basis (n_1,n_2). These processes lead to two kinds of effects: Firstly, an m-electron tunneling process enables charge transfer through m tunnel

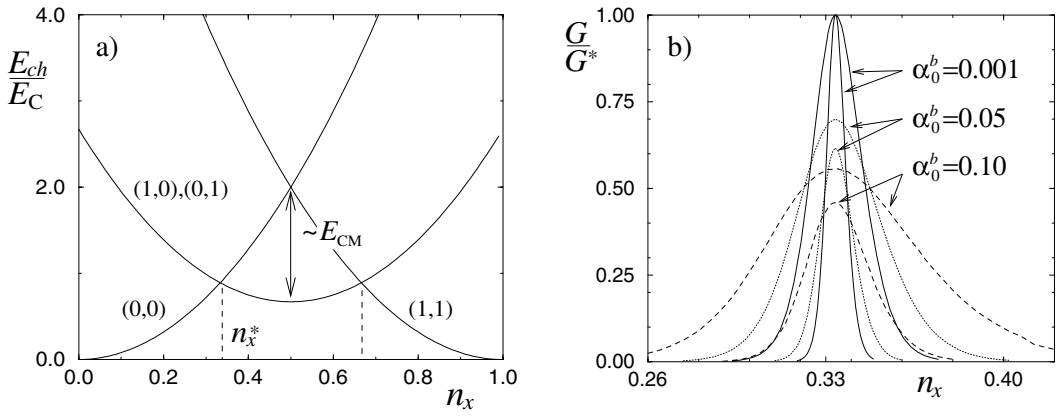

Figure 7: a) Charging energies $E_{\rm ch}(n_1, n_2)$ for the lowest-lying states when $n_{x1} = n_{x2} = n_x$. The linear conductance G displays peaks at the crossing points marked with dashed lines. b) Linear conductance as a function of the gate charge n_x for three values of the tunnel coupling $\alpha_0^b = 0.001, 0.05, 0.10$ (same for all b) as indicated in the figure. The two curves for each α_0^b are for $\ln(T/E_{\rm C}) = -4$ (higher) and -5 (lower).

barriers, despite the Coulomb blockade conditions. The tunneling occurs as a single coherent process involving virtual intermediate states. Figure 5b shows an example of a second-order, or *cotunneling*, process through the two barriers of a SET. These kind of processes lead to a nonvanishing conductance in the Coulomb-blockade regime. Secondly, quantum fluctuations modify the charge states themselves. These changes can be described in terms of the charging energy. Let us illustrate this idea with two examples.

(i) For $\alpha_0^{\rm L,R} \gg \alpha_0^{\rm M}$, the electronic states of the two islands are more strongly coupled to their adjacent leads than to each other. Phenomenologically, the charge states may be visualized to extend across the left and right barriers and to mix with the states in the leads. This enables the system to lower its ground-state energy, i.e., the overall charging energy $E_{\rm C}$, leading to an increase in the curvature of the energy parabolas. As a consequence, the resonant points and hence the conductance peaks are shifted towards each other. The upper curve in Fig. 8a illustrates the shifting of the peak position n_x^* as a function of $\alpha_0^{\rm L,R}$. The reduction of $E_{\rm C}$ has also another effect: it reduces the energy differences Δ_n and, for constant temperature, broadens the peaks. The broadening is clearly seen in the peaks marked with dotted and dashed lines in Fig. 7b; here the peak position remains unchanged due to equal α_0^b and the specifically chosen relative magnitudes of the capacitances.

(ii) In the opposite limit, $\alpha_0^{\rm M} \gg \alpha_0^{\rm L,R}$, the system consists of a strongly coupled subsystem, the two islands, which is only weakly coupled to the leads. Due to the interisland Coulomb interaction, the energy of the charge states $(1, 0)$ and $(0, 1)$ is offset upwards with respect to the states with $n_1 = n_2$, see Fig. 7a. For a large $\alpha_0^{\rm M}$, the electronic

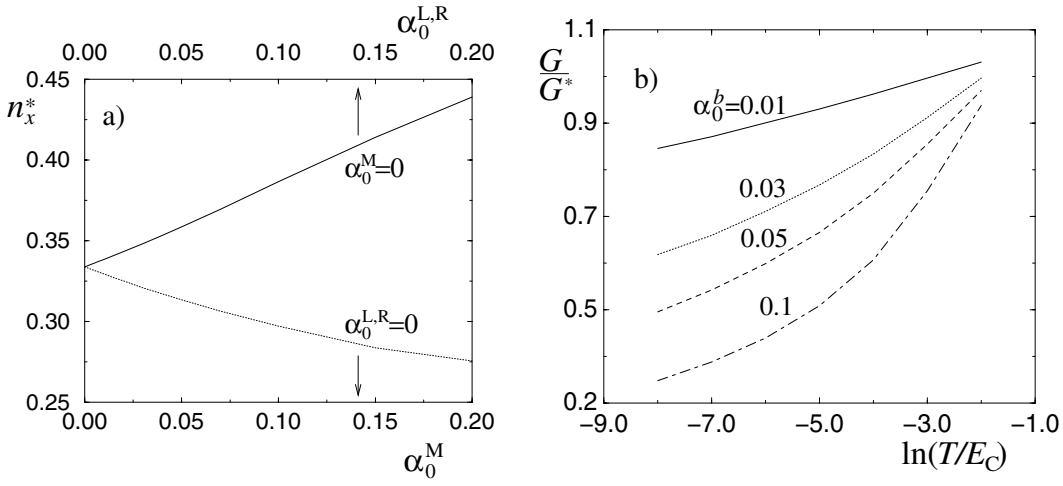

Figure 8: a) When the tunneling couplings vary, the positions of the conductance peaks move. The point n_x^* from a) is plotted for two cases: the upper curve is for $\alpha_0^{\mathrm{L,R}} \gg \alpha_0^{\mathrm{M}} \approx 0$, while the lower curve is for the opposite limit, $\alpha_0^{\mathrm{M}} \gg \alpha_0^{\mathrm{L,R}} \approx 0$. b) Temperature dependence of the conductance maximum for equal α_0^b with its value ranging from 0.01 to 0.10 (from top to bottom).

states on the two islands extend through the middle junction, redistributing the charge between the islands. This enables the system to lower the charging energy for the states with $n_1 \neq n_2$, i.e., to lower the curves $E_{\mathrm{ch}}(1,0)$ and $E_{\mathrm{ch}}(0,1)$ in Fig. 7a with respect to $E_{\mathrm{ch}}(0,0)$ and $E_{\mathrm{ch}}(1,1)$. This has no effect on the curvature of the parabolas determined by E_{C}. As the net effect of increasing α_0^{M}, the resonant points and the conductance peaks are shifted away from each other. The peak position n_x^* as a function of α_0^{M} is shown in the lower curve of Fig. 8a.

The changes in the charging energies may be parametrized as changes in the junction capacitances C_b. These are called renormalized: $C_b \to \tilde{C}_b$. Similarly, also other quantities characterizing the junctions may be renormalized via quantum fluctuations. In particular, the dimensionless conductances $\alpha_0^b \to \tilde{\alpha}^b$ acquire a temperature and an $\alpha_0^{b'}$-dependence ($b' = \mathrm{L}, \mathrm{M}, \mathrm{R}$), thus leading to a reduction in the otherwise temperature-independent conduction peak heights G^*. Figures 7b and 8b show the resulting reduction in the maximum conductance for different tunneling strengths. This phenomenon is intuitively less evident than the energy renormalizations discussed above. The resulting (logarithmic) temperature dependences of $\tilde{\alpha}^b$ and the peak conductance resemble the results obtained for a single metal island [45,47,48]. At low temperatures, the latter model can be mapped onto the so-called multi-channel Kondo model [49] which describes a localized spin $S = \frac{1}{2}$ coupled to a bath of conduction electrons. A thorough analysis of this model predicts a logarithmic temperature dependence of the coupling constants [49,50] similar to the results of Paper I for double-island structures.

Understanding the higher-order effects plays a key role in all SED applications since quantum fluctuations pose more severe limitations on the device operation than, e.g.,

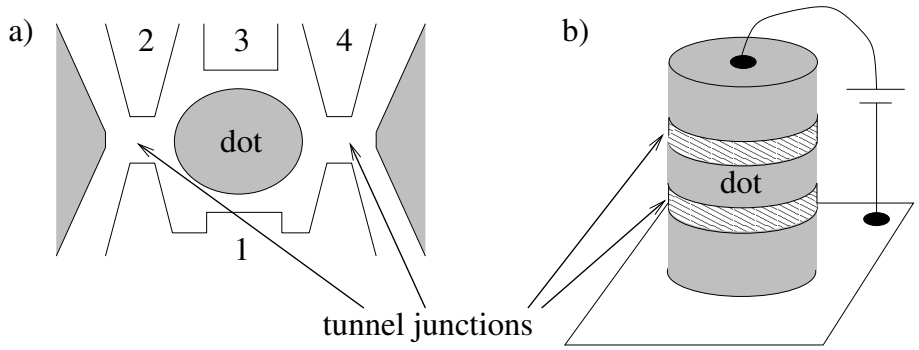

Figure 9: a) Lateral quantum dot defined in a two-dimensional electron gas by applying a negative voltage to the metal gates 1-4 placed on top of the heterostructure. b) Schematic of a vertical dot fabricated by etching away the surrounding heterostructure. In each figure, the quantum dot and the two tunnel junctions are indicated.

thermal fluctuations. In particular, quantum fluctuations determine the fundamental accuracy limits for all single-electron applications. A detailed account of these phenomena in the double-island structures is given in Paper I.

2.3 Semiconductor Quantum Dots

When electrons are confined into a small enough volume, their Fermi wavelength becomes comparable with the system size and the level spacing δ between the single-particle quantum states becomes observable; such structures are called quantum dots. Quantum dots have attracted interest mainly for the specific properties arising from their discrete energy spectrum [12, 51–53], although they can also be used for the single-electron applications discussed above.

Quantum dots can be realized in many different ways, ranging from single atoms under a scanning tunneling microscope (STM) [7] and tiny metal grains [3–6] to sophisticated structures with larger dimensions. The most widely used schemes are based on semiconductor heterostructures, which provide two alternative ways for fabricating dots with dimensions of hundreds of nanometers. In the more common one, a two-dimensional electron gas (2DEG) is structured by a negative voltage applied to metallic finger gates [12, 54–59], see Fig. 9a. The voltage differences between the gates 1 and 2, and 1 and 4 define two tunnel junctions, while the gate 3 serves as a gate electrode which controls the electric potential on the dot. The second scheme uses vertical pilar-like quantum dots formed from a larger heterostructure by etching techniques; the principle is illustrated in Fig. 9b. The electrically conducting layers (gray) serve as the dots and the leads, while the insulating layers (hatched) act as the tunnel barriers [60–62].

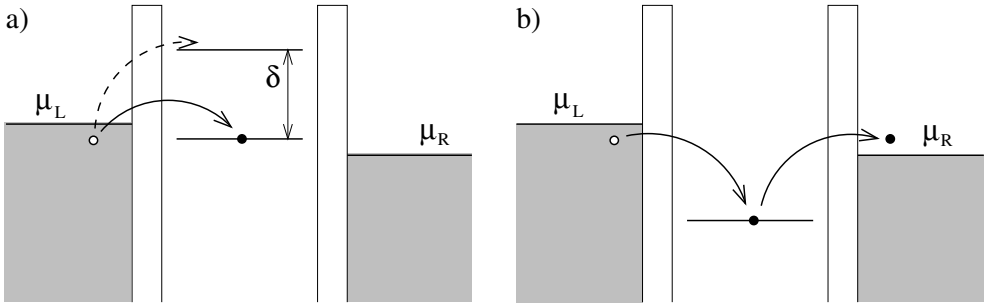

Figure 10: a) Quantum dot with energetically allowed and forbidden single-electron tunneling processes indicated with the solid and dashed arrows, respectively. b) Example of a higher-order tunneling process that contributes to the electron transport in the Coulomb-blockade regime.

Discrete Spectrum

The discrete single-particle spectra of quantum dots resemble those of real atoms, and quantum dots are often referred to as *artificial atoms*. However, in the case of quantum dots, one can control a variety of properties that are inaccessible in real atoms; these include the symmetry of the dot, the single-particle level spacing, and the coupling to the environment. Furthermore, similar to metal islands, one can tune the electrostatic potential on the dot and thereby control the number of electrons. Small changes in the gate voltage – such that n remains constant – can be used to shift the whole level spectrum relative to μ_r. Reviews on the various experimental possibilities can be found, e.g., in Refs. [12, 52].

Similar to metal SED's, the dominant energy scale in quantum dots is usually provided by the charging energy. For typical dots, it is on the order of 1 K and, for $k_{\rm B}T, eV \ll E_{\rm C}$, only two adjacent charge states, n and $n+1$, are involved in the electron transport. In ultrasmall quantum dots, also the level spacing δ may be so large that there is effectively just one or at most two levels close to the Fermi energies in the leads – all the lower (higher) levels are fully occupied (empty).

Electron transport through a quantum dot reflects the discreteness of the dot density of states in a characteristic way: the current can only flow if at least one dot state $|i\sigma\rangle$ lies within the window defined by the bias voltage, $\mu_{\rm L} > \varepsilon_{i\sigma} + \Delta_n > \mu_{\rm R}$; here i and σ denote the level and spin of the electronic states, respectively, and Δ_n accounts for the change in the charging energy. Figure 10a illustrates the possible tunneling processes for $eV \ll \delta$. The differential conductance through the dot, $G = \partial I/\partial V$, displays a peak whenever the chemical potentials cross one of the levels $\varepsilon_{i\sigma}$. This provides a spectroscopic tool for investigating the electronic states in quantum dots [57, 59].

Microscopic Model

The microscopic model for a single energy level coupled to the reservoirs is equivalent to the Anderson impurity model [63]. Generalized for two levels, the Hamiltonian may be expressed as $\mathcal{H} = \mathcal{H}_0 + \mathcal{H}_{\rm T}$ with $\mathcal{H}_0 = \mathcal{H}_{\rm L} + \mathcal{H}_{\rm R} + \mathcal{H}_{\rm D}$ and

$$\mathcal{H}_r = \sum_{kn} \varepsilon_{rki\sigma} c^\dagger_{rki\sigma} c_{rki\sigma} \quad \text{for} \quad r = {\rm L}, {\rm R} \tag{14}$$

$$\mathcal{H}_{\rm D} = \sum_{i\sigma} \varepsilon_{i\sigma} c^\dagger_{i\sigma} c_{i\sigma} + \mathcal{H}_{\rm int} \tag{15}$$

$$\mathcal{H}_{\rm T} = \sum_{rki\sigma} (T^{rk}_{i\sigma} c^\dagger_{rki\sigma} c_{i\sigma} + H.c.). \tag{16}$$

For the special case of at most two electrons occupying the two levels, $n = \sum_{i\sigma} n_{i\sigma} \leq 2$, the interaction term may be written as

$$\mathcal{H}_{\rm int} = U \sum_{i\sigma \neq j\sigma'} n_{i\sigma} n_{j\sigma'}. \tag{17}$$

In ultrasmall dots with just a few electrons in the dots, the energy scale U depends on n and, in general, cannot be described in terms of the charging energy $E_{\rm ch}(n)$. For $n \leq 2$, however, $\mathcal{H}_{\rm int}$ is equivalent to $E_{\rm ch}(n)$ with $U = 2E_{\rm C}$ and the shifted level positions $\varepsilon_{i\sigma} + 2E_{\rm C} - eV_{\rm G}C_{\rm G}/C \to \varepsilon'_{i\sigma}$. In Papers II-V, we focus on the special case $n = 0, 1$, where the interaction effects can be included in the level energies $\varepsilon'_{i\sigma} + \Delta_0 \to \tilde{\varepsilon}_{i\sigma}$ (below we omit the tilde and $\varepsilon_{i\sigma}$ is to be understood to contain the interaction effects).

In the tunneling Hamiltonian $\mathcal{H}_{\rm T}$, the level index i is explicitly conserved in tunneling. This presumably holds for cylinder-shaped vertical structures, where angular momentum is a good quantum number [61], but not necessarily for lateral structures. In the case of a single level in the dot, the index i drops out and $\mathcal{H}$ applies to both realizations. Note also that there is no interlevel coupling in $\mathcal{H}_{\rm D}$. This means that, in accordance with most experimental setups, the tunneling rates are much higher than the rates for intradot relaxation or activation processes.

The tunneling rates through the tunnel junction r into and out of the dot level $\varepsilon_{i\sigma}$ can be obtained by applying the Fermi golden rule: $\Sigma^r_{0\to i\sigma} = \Gamma_{ri}(\omega) f^+_r(\omega)$ and $\Sigma^r_{i\sigma\to 0} = \Gamma_{ri}(\omega) f^-_r(\omega)$ with

$$\Gamma_{ri}(\omega) = \frac{2\pi}{\hbar} \sum_k |T^{rk}_{i\sigma}|^2 \delta(\omega - \varepsilon_{rki\sigma}) \tag{18}$$

and $f^\pm_r = [\exp(\pm\beta(\omega - \mu_r)) - 1]^{-1}$ being the Fermi distribution for reservoir r. A master-equation description based on these rates constitutes the orthodox theory of electron transport through quantum dots [64], c.f., the discussion on SET's above.

Double Quantum Dots

Double quantum dots exhibit a number of interesting properties which are found neither in systems of metal islands nor in single quantum dots. In the weak-tunneling regime,

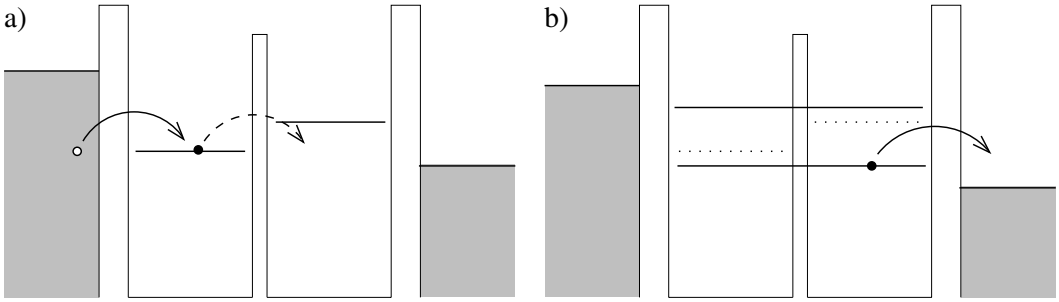

Figure 11: a) An electron can enter the double quantum dot from the left via a sequential tunneling processes indicated with the solid arrow. However, the electron is stuck in the left dot if the states in the two dots are not on resonance. b) For strong interdot coupling, the states in the two dots (dotted) form hybridized molecular-like states (solid) that extend through the central barrier. These extended states enable electron transport through the system.

for example, the electron transport through the system is only possible when the levels $\varepsilon_{di\sigma}$ from both dots ($d = 1, 2$ denotes the dot) are on resonance, i.e., $\varepsilon_{1i\sigma} \approx \varepsilon_{2j\sigma'}$, and lie between the chemical potentials of the leads, see Fig. 11a. This provides improved resolution in the spectroscopic measurements of the dot states [62,65]. As another example, two dots with a strong interdot coupling form an *artificial molecule* with electronic states delocalized between the dots, see Fig. 11b. The coherence of such extended states has been confirmed in recent experiments [66].

The basic properties of double quantum dots may be understood along the lines of Subsec. 2.1 on the charging effects and the above discussion on the discrete spectrum. In Papers II-IV, we consider double quantum dots with such a large level spacing that only a single level in each dot participates in the electron transport. Furthermore, we assume strong intra and interdot Coulomb interactions and neglect doubly occupied states: there can be at most one electron in the *whole* double-dot system. In this case, we may again include the charging effects into the energies $\varepsilon_{d\sigma}$ (level index i may be omitted for single-level dots).

In Paper II, we consider a double quantum dot coupled in a series geometry between two electrodes, see Fig. 12a. The model with the delocalized eigenstates, see Fig. 11b, is equivalent to a single two-level dot in which the states $i = 1, 2$ are the symmetric (bonding) and antisymmetric (antibonding) superpositions of the single-dot states. The transformation to the single-dot model modifies the tunneling Hamiltonian such that the new level index i is *not* conserved in the tunneling. In Papers III and IV, we consider another double-dot model with only capacitive coupling between the dots, see Fig. 12b. We observe that also this Hamiltonian has a single-dot counterpart with two orbital states in the dot. In this case, the orbital index i corresponds to the spatially separated dots and is conserved in the tunneling. In this Thesis, the emphasis is on models where i is conserved.

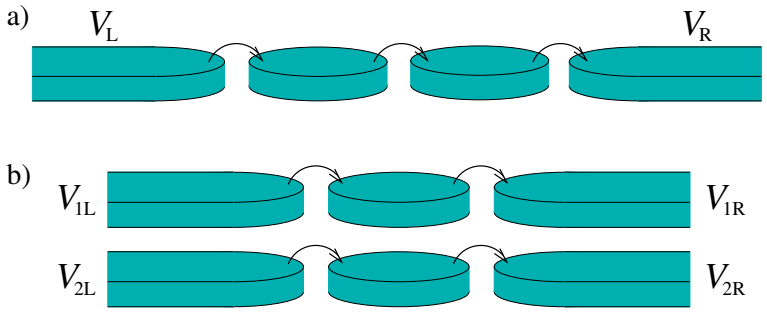

Figure 12: a) Tunneling and b) capacitively-coupled double quantum dots considered in Papers II and III-IV, respectively. Tunneling is possible in junctions denoted by arrows.

2.4 Kondo Effect in Single and Double Quantum Dots

The limitations of the orthodox theory turn out to be even more severe in the case of small quantum dots than for the metal islands [31–33, 62, 67–69]. At low temperatures and/or for strong coupling to the leads, higher-order tunneling processes give rise to quantum fluctuations of the electrons on the dot. The higher-order processes lead to finite lifetime effects and, in some cases, even new many-body states known as the Kondo resonances may emerge [26, 27, 34–38, 70–77].

The experimental verification of the Kondo effect in a semiconductor quantum dot has turned out very challenging due to its sensitivity to decoherence. It was first achieved in 1997 [78] followed by observations of Kondo-like physics in various systems. These accomplishments have triggered an extensive theoretical research, see, e.g., Refs. [79–87].

The low-temperature properties of ultrasmall quantum dot(s) constitute a major part of this dissertation. The results obtained for the linear and nonlinear response regimes yield a comprehensive picture of the Kondo effect in these systems. This subsection outlines the results of Papers II-V, while the theoretical approaches are summarized in Sec. 4.

Single Quantum Dots

Electron transport through a single quantum dot with one spin-degenerate quantum state has been elaborated in Refs. [70–73] for the linear and in Refs. [26, 27, 73, 74, 88] for the nonlinear response regimes. This also consitutes the main subject of Paper V.

The effect of the quantum fluctuations in quantum dots is best demonstrated in terms of the spectral density $A_{i\sigma}(\omega)$, which is the density of states corresponding to the dot state $|i\sigma\rangle$. The current through a quantum dot, for example, is given by [89]

$$I = e \sum_{i\sigma} \frac{\Gamma_{\mathrm{L}i\sigma}\Gamma_{\mathrm{R}i\sigma}}{\Gamma_{\mathrm{L}i\sigma} + \Gamma_{\mathrm{R}i\sigma}} \int_{-\infty}^{\infty} d\omega [f_{\mathrm{R}}(\omega) - f_{\mathrm{L}}(\omega)] A_{i\sigma}(\omega), \tag{19}$$

making $A_{i\sigma}(\omega)$ a central quantity throughout this discussion. The couplings $\Gamma_{ri\sigma}(\omega) = \Gamma_{ri\sigma}$ are assumed independent of energy in the present range of interest. The differential

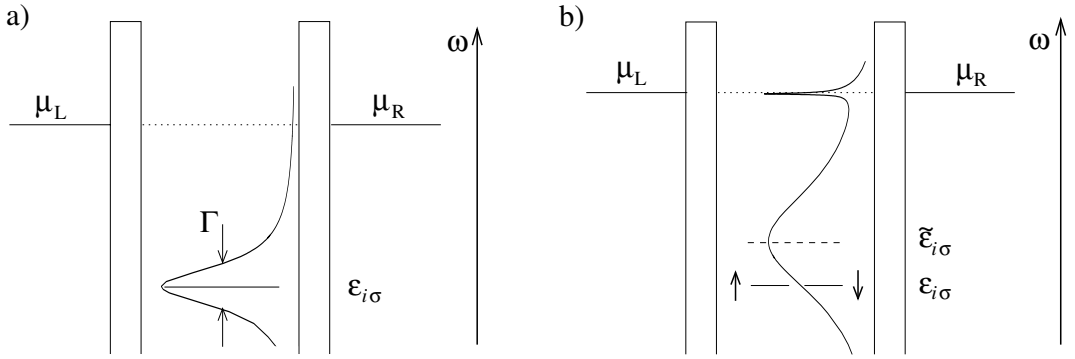

Figure 13: a) Schematic of the Lorentzian-shaped spectral function $A_{i\sigma}(\omega)$ for a single nondegenerate level ε in a small quantum dot. b) $A_{i\sigma}(\omega)$ for a spin-degenerate level at $\varepsilon_{i\sigma}$. The spin degeneracy leads to a renormalization, $\varepsilon_{i\sigma} \to \tilde{\varepsilon}_{i\sigma}$, and further broadening of the level. At low temperatures, a sharp Kondo resonance emerges at μ_r.

conductance $G = \partial I/\partial V$ better reflects the shape of $A_{i\sigma}(\omega)$ (but *not* directly: also $A_{i\sigma}(\omega)$ is voltage dependent) and in the following we focus on the conductance instead of the current.

Let us first consider a single quantum dot with one non-degenerate level (even spin degeneracy is lifted) weakly coupled to two reservoirs. In the weak-tunneling regime, the spectral function $A_{i\sigma}(\omega)$ acquires a delta-function form located at $\varepsilon_{i\sigma}$, and the electron transport through the dot is only possible if the level lies between the chemical potentials of the leads. More precisely, the level needs to lie within the thermally broadened tails of the Fermi distributions in the leads, and the consequent current and conductance display thermally broadened peaks.

Increasing tunneling coupling enhances the higher-order tunneling processes, such as the one shown in Fig. 10b. The resulting quantum fluctuations of the charge through the barriers give rise to a finite lifetime $\tau \sim 1/\Gamma$ and a broadening $\sim \Gamma$ of the dot states. This is manifested by the Lorentzian shape of $A(\omega)$, see Fig. 13a. In experiments, the larger one of $k_{\rm B}T$ and Γ determines the width of the observed conductance peaks. The Lorentzian shape decays only algebraically away from $\varepsilon_{i\sigma}$ and gives rise to a non-vanishing current in the Coulomb-blockade regime.

If the level is spin degenerate, the system is equivalent to the Anderson impurity model, which is known to display richer low-temperature behaviour than just the level broadening, see e.g. Refs. [63, 90, 91]. This is the topic of Paper V. In the temperature regime, $\Gamma \lesssim k_{\rm B}T \ll U$, the spin degeneracy does not lead to any qualitative differences in the transport properties – the conductance displays a series of peaks broadened by $\max\{k_{\rm B}T, \Gamma\}$. Only at temperatures significantly lower than Γ does the difference become evident. Due to the strong onsite Coulomb repulsion, only one electron at a time – with the spin pointing either up or down – is allowed into the dot. The second and

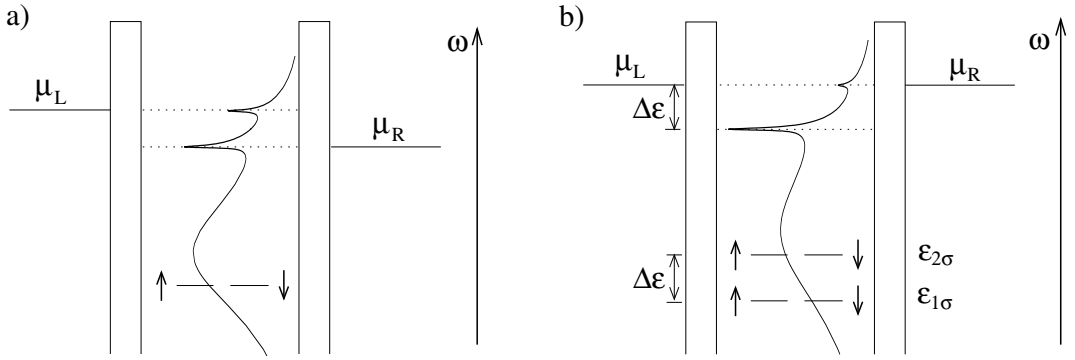

Figure 14: a) A finite bias voltage $eV = \mu_{\rm L} - \mu_{\rm R}$ splits the Kondo resonance in the spectral function $A_{i\sigma}(\omega)$. b) For two spin-degenerate levels at $\varepsilon_{i\sigma}$, $i = 1, 2$, $A_{1\sigma}(\omega)$ displays an additional resonance at $\omega = \varepsilon_1 - \varepsilon_2$.

higher-order tunneling processes, such as the one shown in Fig. 10b, may change the electron in the dot and thereby effectively flip the spin on the dot. When the dot level lies deep below the chemical potentials, the average charge on the dot approaches unity and this model can be mapped onto the (single-channel) Kondo model describing magnetic impurities in metals [90]. In this model, the higher-order processes are interpreted as spin fluctuations.

The spin fluctuations are reflected in the spectral densities in three ways. (i) Firstly, the level is further broadened and (ii) it is renormalized towards higher energies, i.e., $\tilde{\varepsilon}_i > \varepsilon_i$. (iii) For $k_{\rm B}T \ll \Gamma$, the electrons at the Fermi energy in the reservoirs couple with the localized spin to form a new many-body state that screens the localized spin. This new state appears as a sharp resonance in $A_{i\sigma}(\omega)$ at the position of the chemical potentials in the leads, see Fig. 13b. This peaked structure is known as the Kondo resonance and it enhances the conductance through the dot. If $\mu_{\rm L} \neq \mu_{\rm R}$, there is one resonance located at each μ_r, see Fig. 14a. For an increasing bias voltage eV, these resonances are diminished and consequently the differential conductance is reduced. The conductance displays a sharp zero-bias maximum with a characteristic temperature dependence: the peak conductance increases logarithmically with decreasing temperature. Figure 15a shows an example of the resulting conductance with the zero-bias anomaly between two broader peaks; these reflect the actual charge state and correspond to the Coulomb oscillations in Fig. 4b. The temperature dependence is displayed in the inset. Note that the metal structures considered above were related with the *multi-channel* Kondo model and G was found to decrease with decreasing temperature.

Two Levels in a Single Quantum Dot

In some experiments, the estimated level broadenings exceed the level spacing. This indicates that also other dot states ought to play a role in the electron transport. Paper II together with Refs. [84] first considered the effect of an additional level on the Kondo physics; these ideas were later extended in Refs. [92, 93] to cover several electrons and

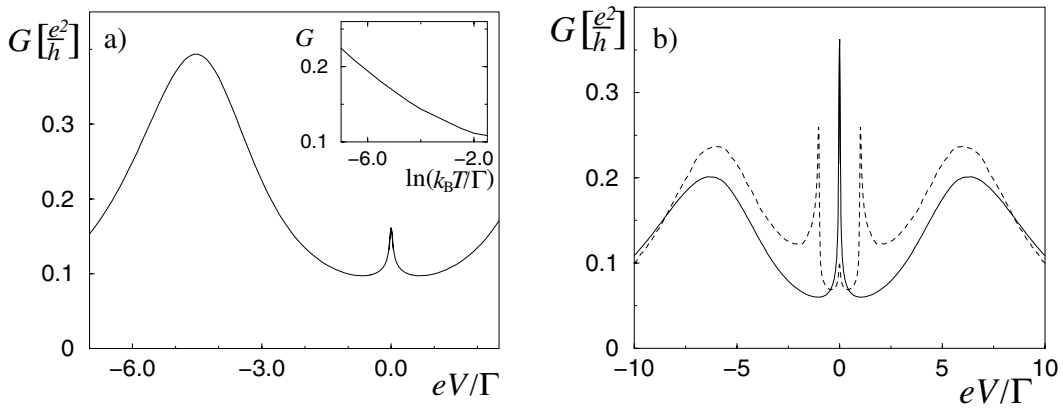

Figure 15: a) Differential conductance G through a quantum dot with one spin-degenerate level at $\varepsilon_{i\sigma} = -3\Gamma$; $k_{\rm B}T = \Gamma/100$. For a left-right symmetric system, the conductance is symmetric with respect to $eV = 0$. The logarithmic temperature dependence of the zero-bias maximum, shown in the inset, is characteristic to the Kondo effect. b) G through a dot with two spin-degenerate levels. The solid and dashed curves correspond to different level separations: $\Delta\varepsilon = \varepsilon_{2\sigma} - \varepsilon_{1\sigma} = 0$ and 0.2Γ, respectively.

levels in the dot and in Papers III and V to a more detailed picture of the two-level model. In these models, the degeneracy of two or more states is crucial for the Kondo effect. Analogies between different models [85, 87, 92–94] as well as recent experimental results [95–98] show that the degeneracy need not be related with the electronic spin.

In Papers II, III, and V, two spin-degenerate orbital states at $\varepsilon_{1\sigma}$ and $\varepsilon_{2\sigma}$ are considered. If these states are degenerate, the level index i can act as a pseudospin and the dot may exhibit Kondo physics even in the absence of the real spin degree of freedom [85, 95]. A prerequisite for this phenomenon is the conservation of i in the tunneling. In this work, the level index is always assumed to be conserved, whereas it is shown in Refs. [47, 99] that the opposite case leads to markedly different physics.

The spectral densities $A_{i\sigma}(\omega)$ exhibit one Kondo-like resonance for each one of the other states – if some of the states are degenerate, the corresponding resonances are enhanced in magnitude. This result holds for nondegenerate orbital states as well as for Zeeman-split spin states. Figure 14b shows an example of $A_{1\sigma}(\omega)$ for one dot state when there is another level at $\varepsilon_{2\sigma} > \varepsilon_{1\sigma}$. The spectral density of the lower level displays an additional resonance located at $\varepsilon_{2\sigma} - \varepsilon_{1\sigma} \equiv -\Delta\varepsilon$. This resonance is reflected in the differential conductance as two satellite peaks occurring symmetrically around the zero-bias anomaly at finite bias voltages. These are shown in Fig. 15b (dashed line). If the level spacing is zero, there is effectively one fourfold degenerate state in the dot and a pronounced zero-bias maximum appears in the differential conductance. Also this is shown in Fig. 15b (solid line).

Double Dots

The degeneracy of states may lead to the Kondo effect also in double quantum dots. This is considered in Papers II-IV. Tunneling-coupled double dots, see Fig. 12a, have been theoretically studied in Refs. [100–106], where only an on-site interaction has been considered. In contrast to this and motivated by experimental facts, we assume a strong interdot Coulomb interaction throughout this work. It was noted above that this facilitates the mapping of certain double-dot models onto that of a single two-level dot with either a conserved or nonconserved orbital index i – in this dissertation i is assumed conserved. The calculations are carried out only for certain charge configurations but the validity range of the results may be extended due to particle-hole symmetry.

In Papers III and IV, the model of two capacitively coupled quantum dots is studied, see Fig. 12b; this model was realized in experiments only quite recently [95]. The level spacing in the dots is assumed large and just one level per dot is considered. Furthermore, only the charge states $n = n_1 + n_2 = 0, 1$ are taken into account. The resulting model is equivalent with a two-level dot with a conserved level index i and the above results obtained for this system apply.

The capacitively coupled double-dot system contains more controllable parameters than its single-dot counterpart, and it opens new possibilities for manipulating the Kondo physics in the system. For example, the transport through one of the dots can be measured, while the parameters of the other dot are altered. Figure 16 shows an example of the resulting rich structure in the linear conductance G_1 through dot 1 when the bias and gate voltages coupled to dot 2 are varied (the picture on the front cover is a bird's eye view of this figure). The plateau with an almost constant conductance corresponds to the top of the zero-bias maximum in the conductance through a single quantum dot in the Kondo regime. For $\varepsilon_{2\sigma} < \varepsilon_{1\sigma}$, the electric transport through dot 1 becomes blocked by an electron in dot 2 – the blockade is lifted once $eV_2 > 2\Delta\varepsilon$. The sharp peak in the center of the figure arises when the levels in the two dots are at resonance and reinforce the mutual Kondo effect. The ridge-like structures behind the peak are due to coincidence of two resonances in $A_{1\sigma}(\omega)$, see Paper III. It is also to be noted that the whole parameter range shown in this figure actually corresponds to the Coulomb-blockade regime.

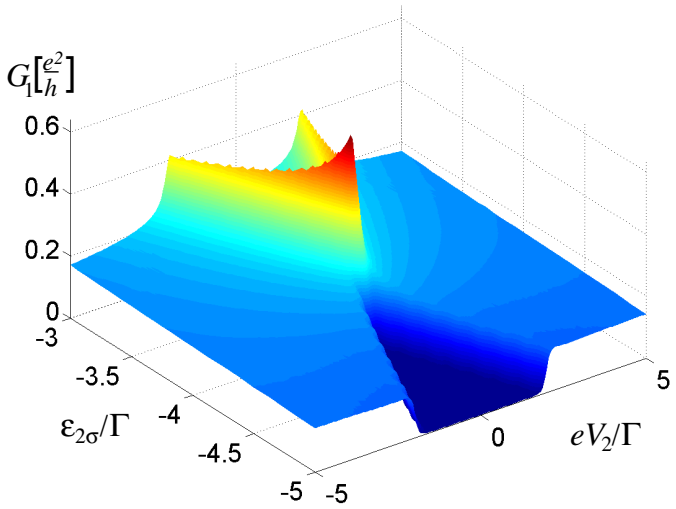

Figure 16: Linear conductance G_1 through one dot in the capacitively coupled double-dot system plotted as a function of the level position $\varepsilon_{2\sigma}$ and transport voltage eV_2 of the other dot. The level $\varepsilon_{1\sigma} = -4\Gamma$ and $k_{\rm B}T = \Gamma/50$.

3 Molecular Magnets – Mn_{12}

The novel magnetic material Mn_{12}-acetate (Mn_{12}) – with the related materials Fe_8 and V_{15} – has recently been the subject of an extensive experimental [18–20, 107–110] and theoretical research [21, 111–121]. The interest in this molecular magnet stems from the experimental indications of macroscopic quantum tunneling (MQT) of magnetization, i.e., quantum mechanical tunneling at a macroscopic level.

One characteristic quantity describing the magnetization dynamics is the relaxation time τ, which characterizes the process of magnetization reversal in an external magnetic field. In the experiments, the relaxation time has been found to display a periodically peaked structure, see Fig. 17b, that is attributed to MQT. Understanding this and other related results is the subject of Paper VI.

In the first subsection below, we introduce a microscopic description of magnetization in Mn_{12} based on molecular spins. In the second subsection, we outline the results obtained for the magnetization dynamics in the regime of thermally activated tunneling.

3.1 Model for the Magnetization

Unlike the SED models whose properties largely derive from the electronic structure of bulk materials, the magnetic properties of Mn_{12} can only be understood by starting from the intramolecular level. Typical experimental samples of Mn_{12} consist of single crystals of identical Mn_{12} molecules. Each molecule has eight Mn^{3+} and four Mn^{4+} ions, which at low temperatures acquire the ferrimagnetic ground state illustrated in Fig. 17a. In the ground state, the molecule behaves as a single spin $S = 10$ with 21 eigenstates of S_z. The magnetic cores of the Mn_{12} molecules are separated by such a thick layer of nonmagnetic matter that, in the first approximation, we may assume the molecular spins independent of each other.

Due to a strong anisotropy along one of the crystalline axes (z-direction), there is a high potential barrier between the opposite orientations of the spin ($S_z = \pm 10$). The Hamiltonian for a single Mn_{12} molecule may be written as $\mathcal{H}_S = \mathcal{H}_z + \mathcal{H}_{\rm T}$ with the first (second) term describing the part that commutes (does not commute) with S_z, the spin component along the easy axis (here the z-direction). The molecular symmetry requires that

$$\mathcal{H}_z = -AS_z^2 - BS_z^4 - g\mu_{\rm B}H_zS_z + O(S_z^6). \tag{20}$$

This expression consists of the potential barrier and a Zeeman term which enables external biasing of the energies – note that, for the nearly perfect crystals used in the experiments, the easy axis is the same for all the molecules [122, 123]. Experimental estimates for the anisotropy constants A and B, as well as for all the other parameters to follow, can be found in Paper VI. Figure 18 shows a schematic of the energy levels E_m (for the eigenstates of $S_z|m\rangle = m|m\rangle$) together with the potential barrier (∼60 K);

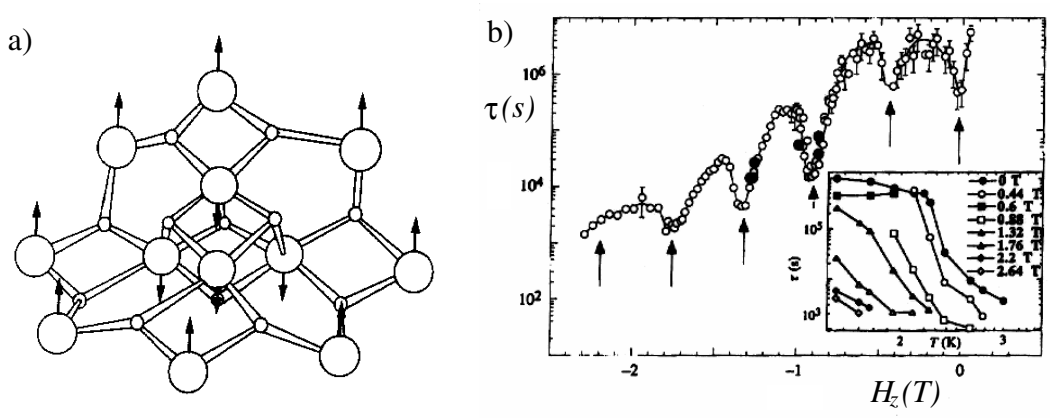

Figure 17: a) Magnetic core of a Mn_{12}-molecule. The large (small) circles denote manganese (oxygen) ions. The arrows correspond to the magnetic moment of the manganese ions in the $S = 10$ ground state. The figure is cited from Ref. [111]. b) Relaxation time of Mn_{12}, see text, as a function of the longitudinal magnetic field H_z; reprinted by permission from Nature (Ref. [20]) copyright (1996) Macmillan Magazines Ltd. The inset displays the measured temperature dependence of the relaxation times in different magnetic fields.

the potential has been drawn as a double well to emphasize the analogy of the model to that of a single electron in a double quantum dot.

The leading-order contributions to the second term in the Hamiltonian (allowed by symmetry) are of the form

$$\mathcal{H}_{\rm T} = -\frac{1}{2}B_4\left(S_+^4 + S_-^4\right) - g\mu_{\rm B}(H_x S_x + H_y S_y). \tag{21}$$

These do not commute with S_z and give rise to tunneling. The B_4 term arises from crystalline anisotropy, while the second term is the Zeeman term corresponding to a transverse magnetic field $H_\perp = H\sin\theta$ (in spherical coordinates, θ is the polar angle away from the z-axis; the azimuth angle is denoted ϕ: $H_x = H_\perp\cos\phi$ and $H_y = H_\perp\sin\phi$).

Similar to the molecular states in double quantum dots (see the previous section) one can solve for the eigenstates $|d\rangle$ of the full spin Hamiltonian $\mathcal{H}_S$. If a pair of states, $|m\rangle$ and $|m'\rangle$, from different sides of the barrier are on resonance, the corresponding eigenstates extend through the barrier; the off-resonant states, on the other hand, are localized into one of the wells. Due to the Zeeman term in Eq. (20), an external magnetic field H_z can be used to tune pairs of states on and off resonance and thereby to control the tunneling coupling. In the absence of the smaller quartic term in Eq. (20) ($B \ll A$), the resonant fields are given by $H_z^n = nA/g\mu_{\rm B} \approx n\cdot 0.42{\rm T}$ (n is an integer) which is in good agreement with the peak positions in Fig. 17b. This suggests that the resonances can be due to the tunneling of identical molecular spins, which is quite remarkable due to the macroscopic number of molecules in the experimental samples. However, the tunneling rates obtained from $\mathcal{H}_S$ are much faster than the observed relaxation rates, and the latter also display a

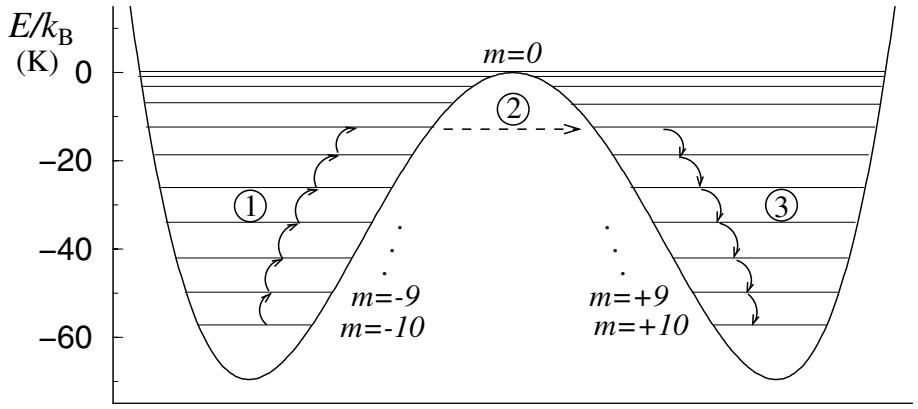

Figure 18: Energy diagram of the 21 eigenstates $|m\rangle$ of S_z. The arrows illustrate the thermally activated tunneling; the magnetization relaxation proceeds as a combination of (1) thermal activation, (2) tunneling, and (3) relaxation.

strong temperature dependence absent in the single-spin model. In the next subsection, these discrepancies are attributed to the spin-phonon interaction.

In the absence of the transverse field, $H_\perp$, there is a selection rule to $\mathcal{H}_\mathrm{T}$: only states $|m\rangle$ and $|m'\rangle$ that are a multiple of four apart are coupled. This would have the immediate consequence that only every second peak in Fig. 17b would be observable. The large peaks in the experimental data do not lend support to such a rule and it turns out that already a tiny transverse field in Eq. (21) is sufficient to reproduce all the peaks [21, 116, 119]. Such a field may arise due to the intermolecular and/or hyperfine interactions within the sample, see below, as well as due to the uncertainty in the precise angle between the external field and the easy axis of the sample. In Paper VI, we assume a constant misalignment angle $\theta = 1^\circ$ of the external magnetic field.

3.2 Magnetization Dynamics

In practise, the Mn_{12} is a far more complicated system than that suggested by the Hamiltonian $\mathcal{H}_S$: the spins interact with each other via the dipolar interaction, with the nuclear spins via the hyperfine interaction, and with the phonons of the surrounding lattice. Experimental evidence shows unequivocally that, in the temperature regime 2–6 K considered here, the spin-phonon interaction plays a key role in understanding the magnetization dynamics [18–20, 108]; the other forms of interaction only affect certain details of the resonances [123]. In this temperature regime, spin relaxation occurs predominantly via thermally activated tunneling: the tunneling takes place between thermally populated and more strongly coupled higher levels.

The theoretical description of the spin dynamics in Mn_{12} range from "minimal" models, assuming as simple a spin Hamiltonian $\mathcal{H}_S$ and a model of the surroundings as possible [21, 111, 113, 114, 116, 119, 120] to more specific models for investigating the role of the

dipolar and/or hyperfine interactions [117, 121, 124], and combinations of these [21, 113, 114, 125]. In many papers and also in Paper VI, the time evolution of the molecular spins is described in terms of a master-equation approach [21, 111, 113, 114, 116, 119, 120, 126]. These theories are sufficient in explaining the general features observed in the experiments. Paper VI extends the existing theories in the following respects: spin dynamics is investigated in the presence of strong transverse magnetic fields and the susceptibility, which has previously only been treated within a phenomenological model [108, 127], is calculated starting from the microscopic Hamiltonian. In this section, we discuss the main results obtained.

Spin-Phonon Interaction and Thermally Activated Tunneling

The spin-phonon interaction is mediated by variations in the local magnetic field induced by lattice vibrations and distortions. A detailed model for the interaction depends on molecular symmetries as well as on the details of the phonon spectrum. Here we adopt the interaction Hamiltonian $\mathcal{H}_{\rm sp}$ of Ref. [119], Eq. (4) in Paper VI, consistent with the tetragonal symmetry of the molecules. To the leading order in the spin-phonon coupling constants, $\mathcal{H}_{\rm sp}$ produces transitions between the different states $|m\rangle$ such that $\Delta m = \pm 1$ or ± 2. The phonons themselves are described as a bath of noninteracting bosons; they are assumed to be plane waves with a linear spectrum and with three modes, two transverse and one longitudinal one.

The magnetization of the whole sample relaxes via inter-well relaxation of the individual molecular spins. The phonon-induced transitions activate and relax the spin along the potential shown in Fig. 18b and lead to a competition between two mechanisms: thermally-activated relaxation *over* and quantum tunneling *through* the barrier. The former is strongly temperature dependent, whereas the latter depends on the longitudinal magnetic field and is suppressed away from the resonances. Figure 19a displays an example of the relaxation rates $\tau^{-1}(H_z)$ obtained (τ is the relaxation time).

The rich structure revealed in Fig. 19a can be elucidated in terms of the eigenenergies E_d of $\mathcal{H}_S$; these are shown in Fig. 19b. The vertical arrows in the figure reflect the effective barrier height U for the relaxing spin. An increasing magnetic field reduces U and thus accelerates the relaxation process. This results in the overall increasing trend of $\tau^{-1}(H_z)$ in Fig. 19a (the dashed curve denotes the rate in the absence of $\mathcal{H}_{\rm T}$). The inset in Fig. 19b – a magnification of the upper left corner of the larger figure – illustrates a few avoided crossings of the eigenenergies. These correspond to the tunnel splittings $\Delta_{m,m'}$ between resonant pairs of states; there are similar although smaller splittings at each crossing. [The tunnel splittings are found by first identifying the corresponding states in the two bases, $|m\rangle \approx |d\rangle$ and $|m'\rangle \approx |d'\rangle$, for off-resonant conditions, and then defining $\Delta_{m,m'} \equiv \min_{H_z} |E_d - E_{d'}|$.] The tunneling accelerates the relaxation process and is reflected in $\tau^{-1}(H_z)$ as a series of sharp peaks. The height of the peaks is determined by the phonon-induced activation rate for reaching the resonant states, while the peak widths are determined by the tunnel splittings.

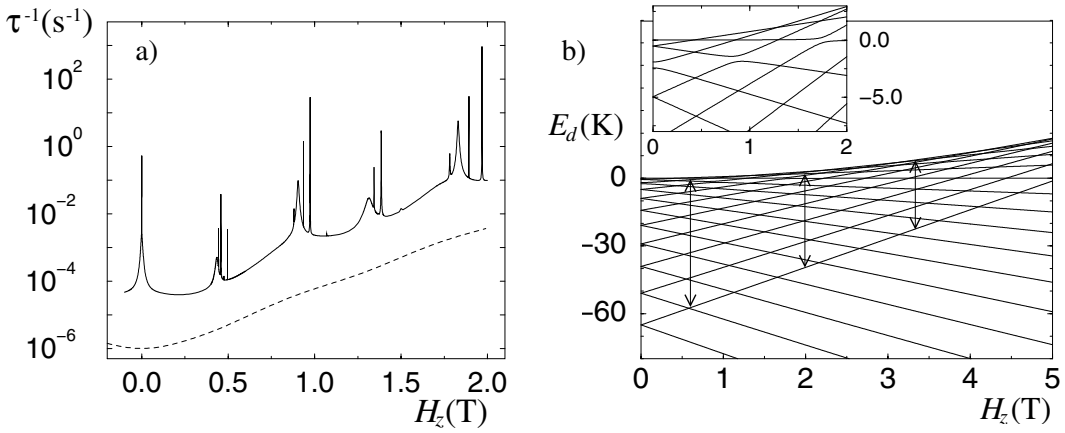

Figure 19: a) Relaxation rate of a single spin $S = 10$ as a function of the longitudinal magnetic field. b) The eigenenergies E_d of the 21 states as functions of H_z. Because of the Zeeman term in $\mathcal{H}_z$, the states corresponding to $m < 0$ and $m > 0$ move up and down, respectively, with increasing H_z thereby reducing the effective barrier height. The inset shows a magnification of the higher energies at low fields – the magnitude of the splittings at the avoided level crossings reflects the tunneling rate.

The sharp peaks correspond to weak tunneling rendering them sensitive to all the possible perturbations in the system. Quantum mechanical tunneling is a coherent process and it may be suppressed by any source of *decoherence* – even the weak spin-phonon interaction is sufficient for suppressing the sharpest resonances. Another effect, which in the actual samples gives rise to decoherence, is the hyperfine interaction between the molecular spin and the nuclear spins of the Mn atoms. The hyperfine interaction is predicted to broaden the resonance peaks and, simultaneously, to reduce their magnitude [113, 114, 117, 125]. As the net effect, only the broadest of the peaks are manifest in typical experimental results, see e.g. Fig. 17b.

The coupling between the molecular spin and the phonon bath could in principle modify the spin states similar to what was found for the quantum dots coupled to electron reservoirs. However, in the present case coupling turns out to be too weak for any significant changes in the spin states, and the most interesting phenomena are found to stem directly from the spin Hamiltonian $\mathcal{H}_S$.

Interference Effects in the Magnetization Tunneling

In Paper VI, a set of experiments is proposed for observing the sharp peaks and, on the other hand, for selective suppression of the visible peaks. These ideas are based on the controllability of $\mathcal{H}_{\rm T}$ by means of an applied transverse magnetic field $H_\perp$.

Figure 20a shows an example of the tunnel splittings as a function of $H_\perp$ for a fixed H_z. The four curves correspond to different angles ϕ in the x-y plane. In contrast to

the simple expectation of monotonically increasing splittings, these are found to exhibit strong oscillations close to the special angles $\phi = \pi(2n+1)/4$ (all features are repeated every $\pi/2$ and we only consider $0 \leq \phi \leq \pi/4$); below we denote these directions as the hard axes of the molecules [125, 128]. A similar phenomenon is known from the related molecular magnet Fe_8: the oscillations are interpreted in terms of a geometrical or Berry phase and the alternating constructive and destructive interference of different tunneling paths [125,128–131]. Figure 20b illustrates the ϕ-dependence of the relaxation rate. The perpendicular field is chosen to be $H_\perp = H_\perp^* = 0.4311$ T such that the tunnel splitting, and thus also the peak in $\tau^{-1}(H_z)$, vanishes for $\phi = 45°$. The value of $H_\perp^*$ is found to be different for each resonance and, since $\Delta_{m,m'}$ is less sensitive to $H_\perp$ away from $H_\perp^*$, the resonances can be manipulated separately.

The main results of Paper VI are concerned with the dynamic susceptibility $\chi(\omega)$ of the Mn_{12}-spins. On the level of a single spin coupled to the phonon bath

$$\chi(\omega; \vec{H}) \approx \frac{\chi_0(\vec{H})}{1 - \omega\tau_1(\vec{H})}, \tag{22}$$

just reflecting the structure found in the relaxation time. This is exemplified in Fig. 20c. Here $\chi_0 = \partial M/\partial H_z$ denotes the stationary susceptibility, $\vec{H}$ is a stationary magnetic field, and ω is the frequency of a weak ac field applied in the z-direction. In the more elaborate case, involving the other spins and the nuclei, we propose susceptibility measurements which would reduce the role of the dipolar interactions – in some cases these induce additional time dependence to the magnetization relaxation. This would facilitate probing the role of the hyperfine interaction in the magnetization dynamics.

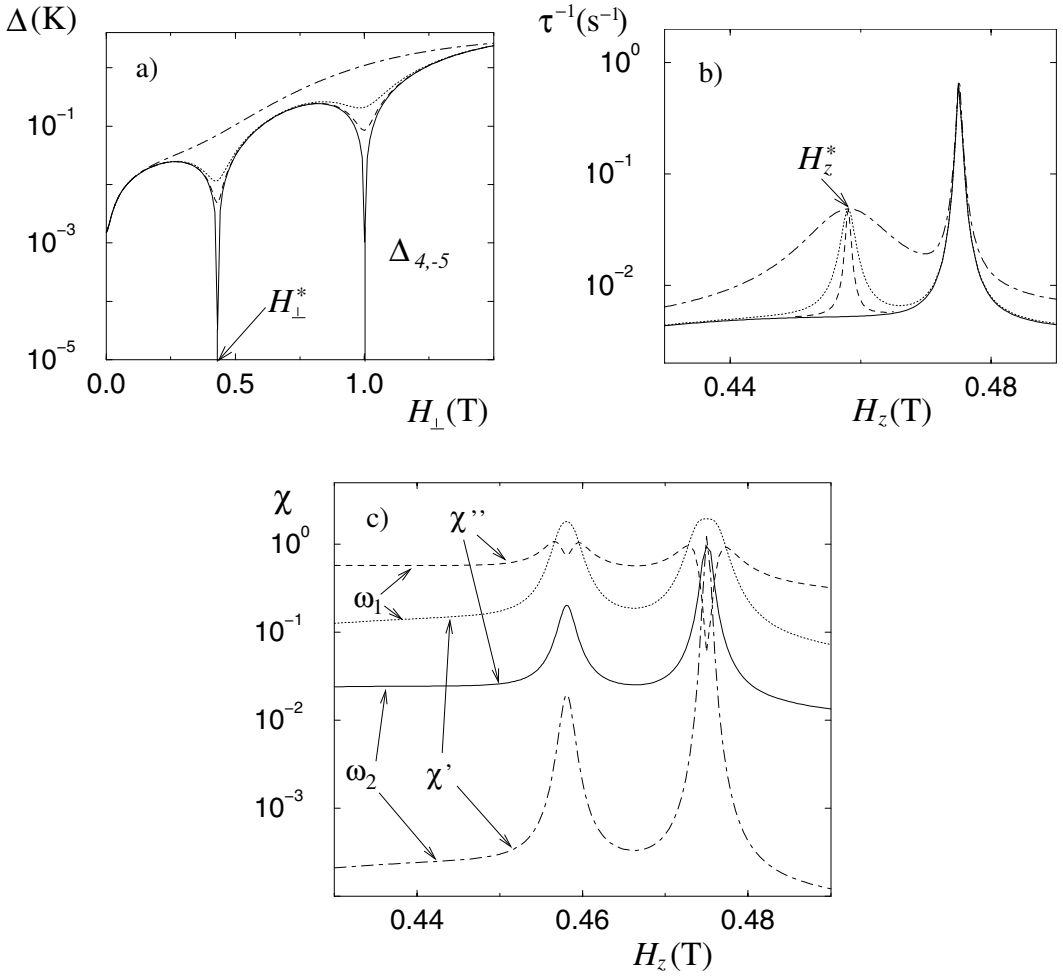

Figure 20: a) Tunnel splittings $\Delta_{4,-5}$ as functions of the *transverse* magnetic field $H_\perp$; $H_z = H_z^* = 0.4581$ T. The curves correspond to different angles ϕ: 0° – dot-dashed, 40° – dotted, 43° – dashed, and 45° – solid. b) Relaxation rate τ^{-1} as a function of the *longitudinal* field H_z for a constant transverse field $H_\perp^* = 0.4311$ T. The four line types correspond to the same four angles as in a). c) Real and imaginary parts of the susceptibility ($\chi = \chi' + i\chi''$) for the same parameters as in b), but with the angle fixed to $\phi = 40°$; the two pairs of curves correspond to the frequencies $\omega_1 = 0.02$ Hz and $\omega_2 = 0.5$ Hz.

4 Real-Time Transport Theory

All the systems discussed in the previous two sections may be considered as realizations of a single class of models: in each of them, there is a small system with a discrete set of states linearly coupled to particle or heat reservoirs. Depending on the specific model, the discrete states may be either single-particle states (quantum dots), many-body charge states (metal islands), or the eigenstates of a spin (Mn_{12}).

In this section, we outline a general theory of such *discrete systems* based on a real-time diagrammatic technique [22, 23, 27] and the reduced density matrix of the discrete system, see e.g. [132]. The real-time formulation enables the description of systems out of equilibrium and it is closely related to the methods used in the context of dissipation [133–135]. This theory forms the basis for all the Papers I-VI, but it also applies to numerous other systems such as an atom irradiated with a laser beam or the spin-boson model, where a spin $S = \frac{1}{2}$ is coupled to a bath of harmonic oscillators.

4.1 Reduced Density Matrix

All the quantities of interest studied in the preceding sections, such as the current, charge, or magnetization, are essentially determined by the states of the discrete system. Due to the coupling, they also depend on all the reservoir degrees of freedom. In this subsection, we derive an effective low-dimensional theory of the system that fully accounts for the coupling but that is expressed in terms of the states $|\chi\rangle$.

Let us consider the generic Hamiltonian $\mathcal{H} = \mathcal{H}_{\rm D} + \mathcal{H}_{\rm res} + \mathcal{H}_{\rm cp}$. The discrete system is described by $\mathcal{H}_{\rm D} = \sum_\chi \varepsilon_\chi |\chi\rangle\langle\chi|$, where $|\chi\rangle$ are the eigenstates of the system. The second term, $\mathcal{H}_{\rm res} = \sum_r \mathcal{H}_r = \sum_{rk} \varepsilon_{rk} c^\dagger_{rk} c_{rk}$, corresponds to the noninteracting degrees of freedom in the reservoirs r, while the third term, $\mathcal{H}_{\rm cp}$, describes the linear coupling between the discrete system and the reservoirs. The coupling term consists of combinations of $c^{(\dagger)}_{rk}$ and $|\chi\rangle\langle\chi'|$, and thus induces transitions between the discrete states (for concrete examples of $\mathcal{H}_{\rm cp}$, see Eqs. (8) and (16) in Sec. 2 and Eq.(4) in Paper VI).

The quantum-statistical expectation value of an arbitrary operator $A(t)$ can be expressed as

$$\langle A(t)\rangle = {\rm Tr}[\rho^{\rm tot}(t)A] = {\rm Tr}[\rho_0^{\rm tot}\ \tilde{T} e^{+i\int_{t_0}^t dt' \mathcal{H}(t')} A\ \ T e^{-i\int_{t_0}^t dt' \mathcal{H}(t')}], \tag{23}$$

where $\rho^{\rm tot}(t)$ is the density matrix of the whole system. Here we assume that the coupling to the environment is switched on at some initial time t_0. At this time, the discrete system is described by the density matrix $p(t_0)$, which is assumed to be diagonal in the eigenbasis $|\chi\rangle$: $p(t_0) = \sum_\chi p^\chi(t_0)|\chi\rangle\langle\chi|$ with $\sum_\chi p^\chi(t_0) = 1$. The reservoirs are not affected by the discrete system and they are for all times described by the equilibrium density matrices $\rho_r^{\rm eq} = \exp[-\beta(\mathcal{H}_r - \mu_r n_r)]/Z^r$ (μ_r is the chemical potential and n_r the total particle number in reservoir r; Z^r is the partition function). For $t \le t_0$, the total density matrix decouples into $\rho_0^{\rm tot} = p^0 \prod_r \rho_r^{\rm eq}$.

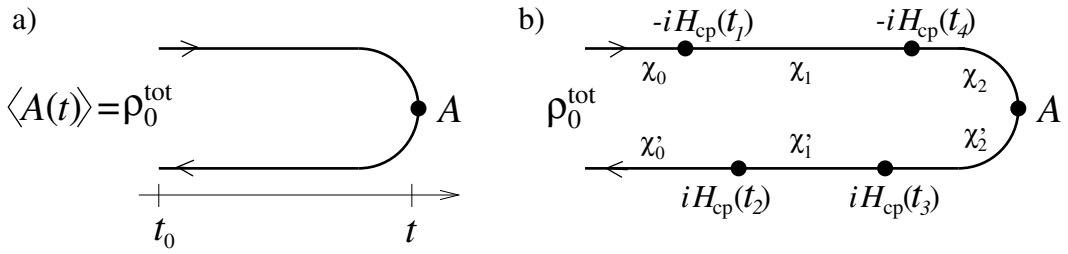

Figure 21: Diagrammatic representation of $\langle A(t)\rangle$ a) before and b) after the expansion in $H_{\rm cp}(t_i)$. In b), $H_{\rm cp}(t_i)$ are represented as vertices and the indices χ_i denote the state of the discrete system. In all the diagrams, the trace over all states is implicitly assumed.

The desired description of the system in terms of the discrete degrees of freedom is attained by first performing the traces over the reservoirs. This is possible due to the factorizability of the initial density matrix. As a result, the states of the discrete system are governed by the reduced density matrix $p(t) \equiv {\rm Tr}_{\rm res}[\rho^{\rm tot}(t)]$. In particular, the expectation value $\langle A(t)\rangle$ of any quantity that only depends on the states $|\chi\rangle$ can be expressed in terms of $p(t)$ as

$$\langle A(t)\rangle = {\rm Tr}[\rho^{\rm tot}(t)A] = \sum_{\chi,\chi'} p^{\chi}_{\chi'}(t)\langle\chi'|A|\chi\rangle. \tag{24}$$

Here $\langle\chi'|A|\chi\rangle$ denotes a matrix element of the operator A. Note that after turning on $\mathcal{H}_{\rm cp}$, it is in general *not* possible to find a basis $|\chi\rangle$, where $p(t)$ would be diagonal; hence, all the elements $p^{\chi}_{\chi'}(t)$ need to be taken into account.

Diagrammatic Technique

The actual evaluation of Eq. (24) and the description of the dynamics of $p(t)$ can be visualized in terms of a diagrammatic language. The starting point is Eq. (23) and its diagrammatic representation in Fig. 21a; the upper (lower) line denotes the propagator directed forward (backward) in time. The coupling part of the Hamiltonian can be separated from the rest of $\mathcal{H}$ in Eq. (23) by adopting the interaction picture with respect to $\mathcal{H}_0 = \mathcal{H}_{\rm D} + \mathcal{H}_{\rm res}$ (indicated with the subscript I)

$$\langle A(t)\rangle = {\rm Tr}\left[\rho_0^{\rm tot}\ \tilde{T}e^{+i\int_{t_0}^{t}dt'\mathcal{H}_{\rm cp}(t')_{\rm I}}A(t)_{\rm I}\ Te^{-i\int_{t_0}^{t}dt'\mathcal{H}_{\rm cp}(t')_{\rm I}}\right], \tag{25}$$

where $(\tilde{T})\ T$ is the (anti-)time-ordering operator. Time ordering along the closed Keldysh-contour in Fig. 21a is expressed compactly as $T_{\rm K}$ and the trace may be written separately for p^0 and $\rho_0^{\rm res}$:

$${\rm Tr}[\rho^{\rm tot}(t)A] = \sum_{\chi}\left[p^0_{\chi}\ {\rm Tr}_{\rm res}\rho_0^{\rm res}\ T_{\rm K}\left(e^{-i\int_{\rm K}dt'\mathcal{H}_{\rm cp}(t')_{\rm I}}A(t)_{\rm I}\right)\right]. \tag{26}$$

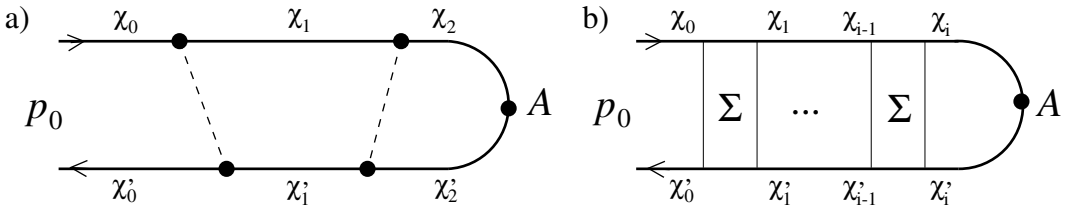

Figure 22: a) Tracing out of the reservoir degrees of freedom couples the vertices and gives rise to interaction lines (dashed). The states $|\chi\rangle$ of the discrete system are indicated. b) Irreducible diagrams are denoted by Σ.

The exponential, expanded in powers of $\mathcal{H}_{\rm cp}$, yields

$$T_{\rm K}\left(e^{-i\int_{\rm K}dt'\,\mathcal{H}_{\rm cp}(t')_{\rm I}}A(t)_{\rm I}\right) = \tag{27}$$
$$\sum_{m=0}^{\infty}(-i)^m \cdot\int_{\rm K}dt_1\int_{\rm K}dt_2...\int_{\rm K}dt_m T_{\rm K}\left(\mathcal{H}_{\rm cp}(t_1)_{\rm I}\,\mathcal{H}_{\rm cp}(t_2)_{\rm I}\,...\,\mathcal{H}_{\rm cp}(t_m)_{\rm I}A(t)_{\rm I}\right),$$

with $t_1 > t_2 > ... > t_m$. Each $\mathcal{H}_{\rm cp}(t_i)_{\rm I}$ is represented as a vertex on the Keldysh contour, see Fig. 21b. The state of the discrete system changes at the vertices and we keep track of this by explicitly assigning states $|\chi\rangle$ to each part of the propagators.

Since $\mathcal{H}_r$ are bilinear in the reservoir operators and the reservoirs are described by equilibrium density matrices, we may use Wick's theorem and contract the reservoir operators in $\mathcal{H}_{\rm cp}(t)$ in pairs of creation and annihilation operators: $\langle c_{rk}^\dagger(t)c_{rk}(t')\rangle_r$ and $\langle c_{rk}(t')c_{rk}^\dagger(t)\rangle_r$. These are the fermionic/bosonic equilibrium correlation functions and they are related to the distribution functions by Fourier transformation. In the diagrammatic representation, the contractions couple pairs of vertices and give rise to interaction lines – the dashed lines in Fig. 22a. The precise functional form of these lines depends on the system under consideration. The sum of all the resulting diagrams describes the time evolution of the reduced density matrix from the initial value $p(t_0) = p^0$ to $p(t)$ at time t.

In the diagrams, one can distinguish between two kinds of time segments based on the criterium of whether a vertical cut through the diagram intersects interaction lines or not. The segments with no interaction lines correspond to free time evolution of the discrete system, while the segments with interaction lines describe interaction processes between the discrete system and the reservoirs. During the interaction segments, the total density matrix is not diagonal with respect to the reservoirs; this means that a coherent process takes place during which the excited quasiparticles do not relax to their equilibrium state. The sum of all irreducible interaction segments with the earliest and latest times t' and t, respectively, is denoted by the self-energy $\Sigma(t,t')$. The time evolution of the reduced density matrix is then governed by the alternating periods of free evolution and $\Sigma(t,t')$, shown in Fig. 22b.

The procedure outlined in this subsection is quite general and can be used in deriving a

set of diagrammatic rules for any of the considered systems – the detailed rules can be found in Refs. [27, 47, 136] for the quantum dots, Ref. [23, 47] for the metal islands, and Ref. [137] for Mn_{12}. Once these rules have been laid down, they can be used in evaluating an arbitrary diagram and, in particular, in calculating $\Sigma(t,t')$. Before discussing this calculation any further, let us first establish a more concrete connection between $p(t)$, $\Sigma(t,t')$, and the dynamical properties of the discrete system.

4.2 Dynamical Quantities

According to Eq. (24), all physical quantities can be expressed in terms of the reduced density matrix $p(t)$. It can be shown that the time evolution of $p(t)$ is governed by the kinetic equation [47, 136]

$$\frac{d}{dt}\, p^{\chi_1}_{\chi_1'}(t) + i(\varepsilon_{\chi_1} - \varepsilon_{\chi_1'})\, p^{\chi_1}_{\chi_1'}(t) = \sum_{\chi_2,\chi_2'} \int_{t_0}^{t} dt'\, \Sigma^{\chi_1,\chi_2}_{\chi_1',\chi_2'}(t,t') p^{\chi_2}_{\chi_2'}(t'). \tag{28}$$

The second term on the left-hand side of Eq. (28) describes the coherent free time evolution of the discrete system, while the integral on the right-hand side describes the dissipative interaction between the discrete system and its environment. These correspond to the two kinds of time segments found in the diagrams. In this subsection, we analyze the kinetic equation assuming that $\Sigma(t,t')$ can be calculated.

In most cases, the integral in Eq. (28) cannot be solved exactly and one has to find some convenient approximation scheme for its evaluation. This procedure can be greatly simplified by two physically motivated assumptions. Firstly, if the Hamiltonian $\mathcal{H}$ is time independent – as is the case in Secs. 2 and 3 and all the Papers I-VI – the kernel only depends on the relative time difference, i.e., $\Sigma(t, t-\tau) = \Sigma(\tau)$. Secondly, the kernel corresponds to coherent processes in the reservoirs; these typically decay rapidly – on some short time scale τ_ϕ – rendering $\Sigma(\tau)$ a fast-decaying function of τ. The reduced density matrix $p(t)$, on the other hand, describes a probability distribution and varies on a longer time scale τ_p. For $\tau_p \gg \tau_\phi$, $p(t')$ remains essentially constant on the scale τ_ϕ, i.e., $p(t') \approx p(t)$ in Eq. (28), and it may be taken out of the integral. This is equivalent to neglecting the memory effects in the interaction, a procedure known as the Markov approximation. The fast decay of the kernel also allows letting $t_0 \to -\infty$.

Assuming that we may make the Markov approximation, the integral in Eq. (28) yields just a time-independent Σ. Consequently, the kinetic equation can be written as $\dot{p}(t) = \frac{\partial p(t)}{\partial t} = -i[\mathcal{H}_{\rm D}, p(t)] + \Sigma p(t) = W p(t)$ and solved for the eigenmodes,

$$\dot{p}^{(i)}(t) = W p^{(i)}(t) = \lambda_i p^{(i)}(t) \quad \Longrightarrow \quad p^{(i)}(t) = p^{(i)}(0) e^{\lambda_i t}. \tag{29}$$

For a system of m states $|\chi\rangle$, there are m^2 eigenmodes. For the systems considered here and for a time-independent Hamiltonian, there is always one mode with $p^{(0)}(t) = p^{(0)}$ and $\lambda_0 = 0$. This corresponds to the stationary state of the system, defined by $\dot{p}(t) = 0$.

The stationary state is described by the master equation

$$-i(\varepsilon_{\chi_1} - \varepsilon_{\chi_1'})\, p^{\chi_1}_{\chi_1'} + \sum_{\chi_2,\chi_2'} \Sigma^{\chi_1,\chi_2}_{\chi_1',\chi_2'}\, p^{\chi_2}_{\chi_2'} = \sum_{\chi_2,\chi_2'} W^{\chi_1,\chi_2}_{\chi_1',\chi_2'}\, p^{\chi_2}_{\chi_2'} \tag{30}$$
$$= \sum_{\{\chi_2,\chi_2'\}\neq\{\chi_1,\chi_1'\}} [W^{\chi_1,\chi_2}_{\chi_1',\chi_2'}\, p^{\chi_2}_{\chi_2'} - W^{\chi_2,\chi_1}_{\chi_2',\chi_1'}\, p^{\chi_1}_{\chi_1'}] = 0 \ \text{ for all } \chi_1, \chi_1'.$$

The other modes correspond to deviations from the stationary state and decay at the rate $\tau_i^{-1} = -Re(\lambda_i)$ ($\tau_i^{-1} > 0$ for all $i \neq 0$). The eigenmodes and relaxation times allow us to describe the full time evolution of the system from an initial out-of-equilibrium state $p(t_i) = \sum_i c_i\, p^{(i)}$ to the stationary state.

After these general considerations, let us be more specific and relate the above results to a few physical quantities relevant to the SED's and Mn_{12}. For example, the average charge in the former and the magnetization in the latter can be written in terms of the diagonal elements $p_\chi(t) = p^\chi_\chi(t)$ as $\langle n(t)\rangle = \sum_\chi p_\chi(t) n_\chi$ and $M(t) \equiv \langle m(t)\rangle = \sum_\chi p_\chi(t) m_\chi$, respectively. For a time-independent Hamiltonian, the time dependences are solely due to the relaxation of $p(t)$ towards the stationary distribution $p^{(0)}$. The eigensolutions of the kinetic equation fully describe the transient period and, in particular in the case of Mn_{12}, are sufficient for the description of the relaxation behaviour observed in the experiments. Furthermore, in Paper VI the dynamical susceptibility of the Mn_{12}-spin, $\chi(\omega)$, is related to the slowest mode with the longest relaxation time τ_1 by Eq. (22).

Equation (24) indicates that the description of an arbitrary physical quantity requires the use of all the matrix elements $p^\chi_{\chi'}(t)$. However, the conservation of charge, spin, or the tunneling-channel index restricts the system dynamics to the diagonal states $p_\chi(t) = p^\chi_\chi(t)$. This is the case in all the SED's considered in this Thesis. The tunneling current through the SED's can be written in the general form, i.e., without the Markov approximation, as

$$I_r(t) = -e \sum_{\chi,\chi'} \int_{t_0}^{t} dt'\, \Sigma^r_{\chi,\chi'}(t,t')\, p_{\chi'}(t'). \tag{31}$$

The *current rate* $\Sigma^r_{\chi,\chi'}(t,t')$ is a subset of the full kernel $\Sigma_{\chi,\chi'}(t,t')$ consisting of those terms where the number of electrons in the reservoir r is changed [27]. In Papers I–V, the emphasis is on the transport properties in the stationary limit $t_0 \to -\infty$ and $p_\chi(t) = p_\chi$. In this case, the density matrix can be taken in front of the integral in Eq. (31) and

$$I_r = -e \sum_{\chi,\chi'} \Sigma^r_{\chi,\chi'} p_{\chi'}, \tag{32}$$

where $\Sigma^r_{\chi,\chi'}$ denotes the integral over t'.

Equations (28)–(32) are to demonstrate that all the quantities of interest can be calculated from the knowledge of $\Sigma(t,t')$. In some cases, it can be more convenient to proceed differently. In Papers II–V, for example, the current through the quantum dots is first related to the spectral functions $A_{i\sigma}(\omega)$, which in turn are evaluated by means of the diagrams.

4.3 Quantum Fluctuations

The foregoing analysis shows that the dynamical properties of the discrete system interacting with its surroundings are determined by the integration kernel $\Sigma(t,t')$. The evaluation of this kernel for the different systems and coupling strengths constitutes a major part of This thesis, and is the subject of the present subsection.

In the following, we first consider a systematic perturbation theory (in the reservoir coupling g) as an extension to the golden-rule rates in the weak-coupling regime. For stronger coupling various higher-order effects become important, rendering the perturbative expansions cumbersome. Below, we discuss two nonperturbative approaches – the resonant-tunneling approximation and the real-time renormalization group technique – better suited for the strong-coupling regime.

Perturbation Theory

A consistent perturbative description of the system dynamics can be formulated by expanding all quantities in powers of the coupling constant g. It turns out that only even powers of g occur in the expansions and, in what follows, the order i actually stands for $O(g^{2i})$. For example, the probabilities and rates become

$$p = p^{(0)} + p^{(1)} + p^{(2)} + \cdots \tag{33}$$

$$W = W^{(1)} + W^{(2)} + W^{(3)} + \cdots . \tag{34}$$

The prerequisite for this procedure is the convergence of the series, i.e., that $g < 0$. Furthermore, for $g \ll 1$, $\sum_{i=0}^{\infty} A^{(i)} \approx \sum_{i=0}^{j} A^{(i)}$ for some j. The actual expansion parameters in Papers I-VI are α_0 for the metal SED's, Γ for the quantum dots, and A^2 for the Mn_{12}-spin [from Eq. (20); this is related to the spin-phonon coupling constant].

The kinetic equation, Eq. (28), and the master equation, Eq. (30), can also be expanded and they have to hold separately in every order of the expansion. In particular, in the stationary case

$$p\,W = p^{(0)}W^{(1)} + (p^{(0)}W^{(2)} + p^{(1)}W^{(1)}) + \cdots = 0 \tag{35}$$

$$\Rightarrow \sum_{j=0}^{i-1} p^{(j)}W^{(i-j)} = 0 \qquad \text{for all } i. \tag{36}$$

In addition, $\mathrm{Tr}[p] = \mathrm{Tr}[p^{(0)}] + \mathrm{Tr}[p^{(1)}] + \cdots = 1$ leading to $\mathrm{Tr}[p^{(0)}] = 1$ and $\mathrm{Tr}[p^{(i)}] = 0$ for $i \geq 1$. The rates Σ can be evaluated in all orders in terms of the diagrams, and the terms $W^{(j)}$ and $p^{(i)}$ can be solved iteratively from the knowledge of $\Sigma^{(j)}$, for $j \leq i$, and $p^{(k)}$, for $k < i$. All the observables can be expanded in a similar fashion.

In the lowest order, $O(g^2)$, only diagrams with one line contribute to Σ; Fig. 23a shows an example of such a diagram. The sum of these terms makes up $\Sigma^{(1)}$ and reproduces the golden-rule rates, e.g., Eqs. (4) and (18) in Sec. 2. The lowest-order terms are characterized by the requirement of energy conservation and, at low temperatures and

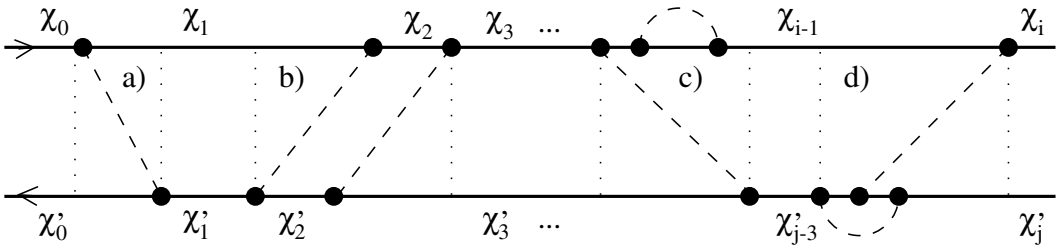

Figure 23: Diagram a) represents a contribution to $\Sigma^{(1)}$ and b)-d) contributions to $\Sigma^{(2)}$. The diagrams c) and d) give rise to renormalization of the levels and the coupling constants, respectively. The vertical dotted lines are guides for the eye in distinguishing the irreducible diagrams a)-d).

away from points of degeneracy, they may be exponentially suppressed. This leads, e.g., to the Coulomb-blockade effects. In such regimes, the quantum corrections arising from the higher-order terms may become dominant; for small g's, the second-order, or $O(g^4)$, term is the most prominent since the higher powers are diminished for $g \ll 1$. The higher-order terms are particularly important for SED's considered, whereas in Mn_{12} these turn out negligible and the lowest-order terms are sufficient for explaining the experiments.

In the second order, there are three kinds of contributions to the transition rates; examples of the respective diagrams are shown in Figs. 23b-d.

(i) Firstly, transitions suppressed in the lowest order can take place via virtual intermediate states $|\chi'\rangle$. Figures 5b and 10b illustrate such processes in the SED's. The rates for these second-order processes are similar to the rates $\Gamma_{i\to f}$ obtained in the standard perturbation theory in $O(g^4)$ for transitions between between the initial and final states, $|i\rangle$ and $|f\rangle$, respectively:

$$\Gamma_{i\to f} = \frac{2\pi}{\hbar}\left|\sum_{\chi'\neq i}\frac{\langle\chi_f|\mathcal{H}_{\rm cp}|\chi'\rangle\langle\chi'|\mathcal{H}_{\rm cp}|\chi_i\rangle}{\varepsilon_{\chi'}-\varepsilon_i}\right|^2\delta(\varepsilon_i-\varepsilon_f) \tag{37}$$

(in the general case, the delta function is replaced by an integral expression with both real and imaginary parts). These correspond to the "classical" rates calculated in Refs. [42–44] for the cotunneling through SED's. Similar to Eq. (37), these rates diverge for $\varepsilon_{\chi'}\to\varepsilon_i$, i.e., when approaching resonances. This deficiency is only remedied by the systematic account of all contributions to $\Sigma^{(2)}$, see below, as well as the corrections $p^{(1)}$ in Eqs. (33) and (35) [45,46].

The other two second-order contributions correspond to renormalization terms. In terms of the diagrams, these contain *bubble* diagrams, which start and end on the same propagator, see Figs. 23c and d. (ii) The bubbles, which do not enclose vertices, lead to propagator/energy renormalization: $\varepsilon_\chi \to \tilde{\varepsilon}_\chi = \varepsilon_\chi + \delta\varepsilon_\chi$. The possible imaginary part of the energy $\tilde{\varepsilon}_\chi$ corresponds to the broadening of the corresponding state. (iii) On the

other hand, the bubbles that do enclose one of the vertices lead to renormalization of that vertex and, consequently, the coupling constants: $g \to \tilde{g} = g + \delta g$. The renormalization terms can be expressed in terms of lower-order rates with the bare parameters replaced by the renormalized ones. In the present case, the renormalization contributions to $\Sigma^{(2)}$ are found by inserting $\tilde{g}$ and $\tilde{\varepsilon}_\chi$ to the golden-rule rates. A systematic second-order calculation of the electron transport through two metal islands is presented in Paper I.

An advantage of the systematic perturbative approach is that it accounts for all the diagrams in each order. Each diagram corresponds to a specific transition process or renormalization term, and one can easily keep track of the processes included in the theory. However, the number of contributions to $\Sigma^{(i)}$ increases rapidly in higher orders and, for increasing g's, it becomes more convenient to consider some nonperturbative approaches.

Resonant Tunneling Approximation

The description of a strong reservoir coupling requires diagrams up to high orders in g. In this subsection, we introduce the so-called resonant-tunneling approximation [22, 23], which accounts for certain *classes* of diagrams up to *all* orders in g. This is achieved in terms of a partial resummation of diagrams in the spirit of the Dyson equation. The resonant-tunneling approximation has been employed in Papers II-V to describe electron tunneling through quantum dots but, despite its suggestive name, it can be applied to other kinds of couplings as well (the name stems from Refs. [22, 23], where this approximation was first used in describing on-resonance electron transport through SED's).

The resonant-tunneling approximation is formally defined by the following requirement when selecting the diagrams to be included in the self-energy $\Sigma(t, t')$: at any time, a vertical cut through the diagram may cut at most two interaction lines. In more physical terms, all those processes are accounted for where there is at most one particle-hole excitation present in the reservoirs. The calculations presented in Papers II–V are based on a set of auxiliary functions which have been found convenient in calculating $\Sigma(t, t')$. In particular, $\Sigma(t, t')$ can always be expressed in terms of the diagrams/functions $\Phi(t, t')$ defined as the sum of all the irreducible diagrams, where the rightmost interaction line is left uncoupled, see Fig. 24. In what follows, we discuss two ways of calculating $\Phi(t, t')$.

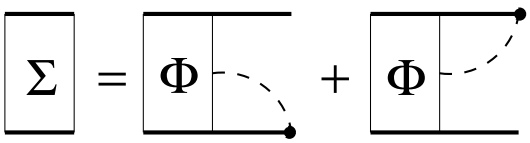

Figure 24: Self-energy can always be expressed in terms of the auxiliary functions $\Phi(t, t')$.

Let us start with the simpler one of the two and assume that the rightmost interaction

line extends through the whole diagram to the initial time t'. Other processes may take place between the times t' and t but, within the resonant-tunneling approximation, only in a sequence of single interaction lines. This approximation is illustrated in Figs. 25 and 26, which define two further functions/diagrams, $\sigma(t,t')$ and $\pi(t,t')$, which can be evaluated analytically within the resonant-tunneling approximation. The former consists of all the possible time segments where there is a second interaction line, while the latter is the sum of all sequences of $\sigma(t,t')$. For convenience, in what follows we assume that all the expressions only depend on the relative time coordinate $t-t'$ and change into the energy representation obtained via Fourier transformation.

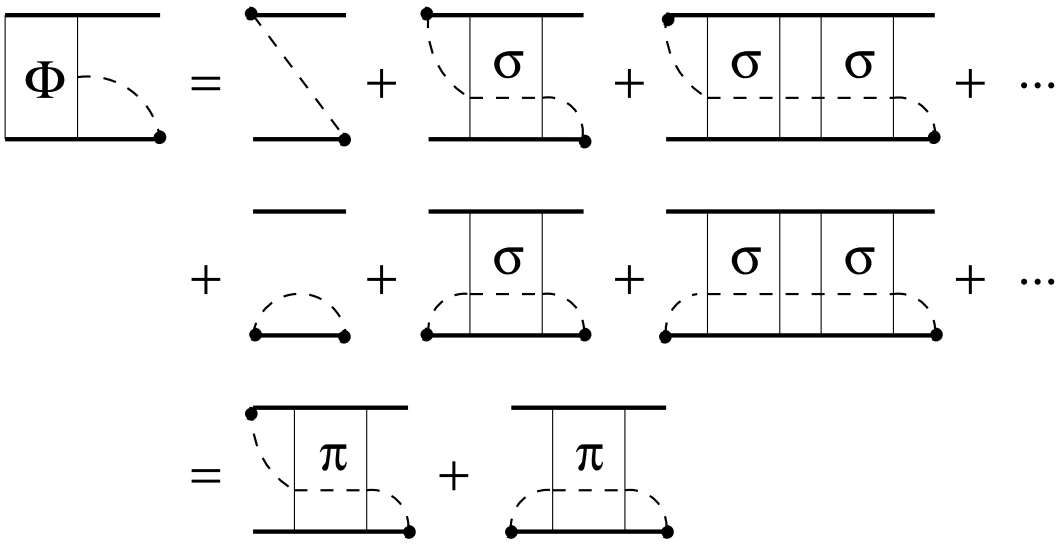

Figure 25: One possible approximation for $\Phi(t,t')$ that includes an infinite number of diagrams. In each diagram, one interaction line runs from t' on the left to t on the right; the time segments with two interaction lines are denoted by $\sigma(t,t')$.

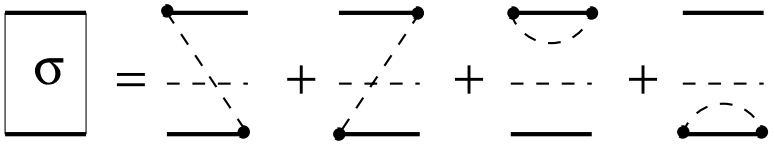

Figure 26: Within the resonant-tunneling approximation, the function $\sigma(t,t')$ is given by four terms. This function is used in Fig. 25 for constructing $\Phi(t,t')$.

The above approximation scheme for calculating $\Phi(\omega)$ and Σ is equivalent to the equation-of-motion method, see e.g. Ref. [138], and it extends the notion of the propagator/energy renormalization to all orders in g. Let us illustrate the consequences with an example from Papers II and III, and consider a single quantum dot with two levels and at most one electron in it. In this case, the interaction lines correspond to tunneling electrons, and Σ, obtained from $\Phi(\omega)$, yields the transition rates between the states $|0\rangle$ (empty dot), $|1\uparrow\rangle$, $|1\downarrow\rangle$, $|2\uparrow\rangle$, and $|2\downarrow\rangle$. Let us further specify that the tunneling line running

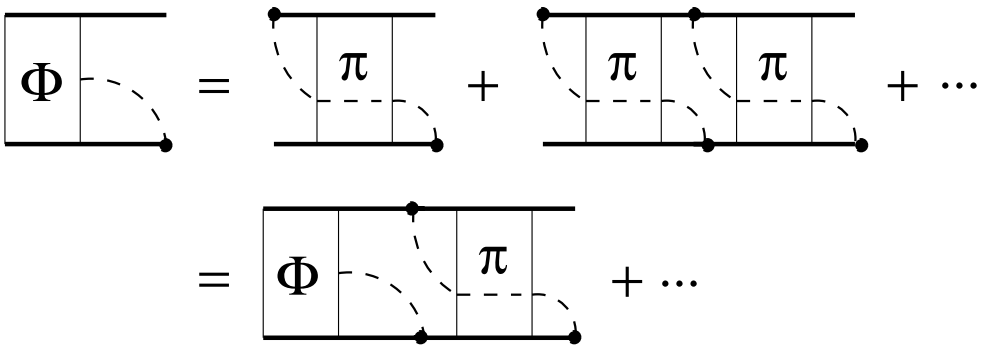

Figure 27: All diagrams compatible with the resonant-tunneling approximation can be accounted for by solving a self-consistent group of equations for $\Phi(t,t')$.

through the diagrams in Fig. 25 corresponds to the tunneling of an electron from the reservoir r into the dot state $|i\sigma\rangle$; the line is then given by the function $\gamma^+_{ri\sigma}(\omega)$ introduced in the context of golden-rule rates in Subsec. 2.3. The whole series of terms in Fig. 25 can be expressed in terms of $\gamma^+_{ri\sigma}(\omega)$ and $\sigma_{ri\sigma}(\omega)$ and we obtain

$$\Sigma^r_{i\sigma,0} = 2i\ \mathrm{Im} \int_{-\infty}^{\infty} d\omega\ \frac{\gamma^+_{ri\sigma}(\omega)}{\omega - \varepsilon_{i\sigma} - \sigma_{ri\sigma}(\omega)}. \tag{38}$$

In the weak-coupling limit, $\sigma_{ri\sigma}(\omega) \to -i\eta$ (at the end we let $\eta \to 0^+$) leading to a delta function located at the pole of the denominator, $\delta(\omega - \varepsilon_{i\sigma})$. In this limit, the result is just the golden-rule rate: $\Sigma^r_{i\sigma,0} = 2\pi\gamma^+_{ri\sigma}(\varepsilon_{i\sigma})$. The poles in the denominator in Eq. (38) correspond to the states of the discrete system also in the more general case where the reservoir coupling gives rise to nontrivial self-energies $\sigma_{ri\sigma}(\omega)$: the real part of $\sigma_{ri\sigma}(\omega)$ shifts or renormalizes the level $\varepsilon_{i\sigma}$ entering the above delta function, whereas its imaginary part broadens the delta function itself. The magnitude of the broadening is found to be proportional to the reservoir coupling strength Γ and it corresponds to the inverse lifetime of the dot states. The energy dependence of the self-energies may lead to further nontrivial effects: for some $\varepsilon_{i\sigma}$, there may be more than just one pole indicating the emergence of *new* many-body states. The Kondo resonance is an example of such a state.

Comparison of Figs. 23b and 25 shows that the above approximation does not include even all the second-order terms. In Refs. [22–27,136] and Papers II-V, another scheme is employed, which accounts for all the diagrams compatible with the resonant-tunneling approximation. The idea underlying these calculations is illustrated in Fig. 27. In the spirit of the Dyson equation, $\Phi(\omega)$ is solved from a self-consistent group of equations. This procedure includes further classes of diagrams [not included in $\sigma(\omega)$ and $\pi(\omega)$] and improves the quantitative results obtained.

The resonant-tunneling approximation is the main approach used in this thesis in the context of quantum dots and the Kondo effect. It is best suited for systems with a small number of states and not too strong couplings. In some systems, an increasing coupling

strength increases the number of relevant states deteriorating the quantitative prediction power of the resonant-tunneling approximation for large g's. This is the case, e.g., in the double-island system studied in Paper I. This problem can be solved by the real-time renormalization-group technique to be introduced next.

Real-Time Renormalization Group Theory

All the foregoing approximations are based on selecting the most relevant diagrams for a given system and parameter regime. In this subsection, a renormalization-group (RG) technique is outlined, which ideally accounts for *all* the states and transition processes; for an introduction see Ref. [139]. Unlike the previous RG approaches applied to, e.g., the single-electron box [49, 50], the present theory is formulated on the Keldysh contour and it accounts for nonequilibrium effects as well as finite lifetime broadening of the states [140, 141].

The objective in the real-time RG is to find an effective low-energy description that accounts for all the processes corresponding to the energy scales below some high-energy cutoff E_c. In the real-time representation adopted in the following, this corresponds to time scales above the temporal cutoff $t_c \sim 1/E_c$. This is achieved by considering the propagator $T\exp[-i\int dt\mathcal{H}(t)]|_{t_c}$ and requiring that it remains invariant upon the change $t_c \to t_c + \delta t_c$:

$$Te^{-i\int dt\mathcal{H}(t)}\Big|_{t_c} \to Te^{-i\int dt\mathcal{H}'(t)}\Big|_{t_c+\delta t_c}. \tag{39}$$

The change in t_c is accounted for by the modifications occurring in the Hamiltonian $\mathcal{H}'$. The possible changes include parameter renormalizations and the generation of new terms. The cutoff t_c is increased in infinitesimal steps from an initial t_c^i to some final t_c^f, and the effect is incorporated into the Hamiltonian. Once $t_c > 1/\varepsilon_\chi$ for some high-energy state $|\chi\rangle$, the influence of $|\chi\rangle$ is already contained in the parameters describing the lower states. Therefore, the high-energy states can be systematically omitted, or integrated out, from the Hamiltonian. At the final stage, when t_c reaches t_c^f, the full dynamics of the system is described by the remaining low-dimensional Hamiltonian.

Examples of the parameter renormalization have already been encountered in the preceding subsections as the renormalization of the energies, $\varepsilon_\chi \to \tilde{\varepsilon}_\chi$, and the coupling constants, $g \to \tilde{g}$. In the parameter regimes considered in Papers I, IV, and V, the emergence of any new terms can be neglected and only t_c-dependent system parameters are obtained. This dependence can be formulated as a set of differential equations (flow equations)

$$\frac{\partial\varepsilon_\chi}{\partial t_c} = F(\{\varepsilon_\chi, g\}; t_c) \tag{40}$$

and

$$\frac{\partial g}{\partial t_c} = G(\{\varepsilon_\chi, g\}; t_c), \tag{41}$$

where F and G are functions of all the system parameters and the cutoff t_c. In practice, the RG procedure corresponds to the integration of the flow equations from t_c^i to t_c^f.

The RG equations (40) and (41) are system specific and need to be derived separately for each system. This derivation involves evaluation of real-time diagrams and, in so doing, some approximation procedure usually needs to be employed. Consequently, the approach presented in Refs. [140,141] is suitable for some systems, but it fails to describe, e.g., the Kondo effect in quantum dots. In Papers I and IV, two simplified versions of the general RG have been employed in describing electron transport through metal islands and quantum dots, respectively. Both versions are based on equilibrium conditions and, for small bias voltages and strong tunneling couplings, they yield far better results than any of the other approaches discussed in this section.

5 Discussion

This dissertation focuses on the quantum dynamics of three mesoscopic systems: (i) metallic and (ii) semiconductor single-electron devices (SED's), and (iii) the molecular magnet manganese acetate (Mn_{12}).

In the first and major part of the Thesis (Papers I-V), the focus is on various SED configurations. The concepts underlying all existing SED applications are based on the orthodox theory of Coulomb blockade which neglects all the higher-order tunneling processes beyond sequential tunneling. In the recent experiments, this level of description has proved inadequate and a thorough investigation of quantum fluctuations in SED's has been called for. Such an investigation constitutes the subject of Papers I-V.

In Paper I, metallic double-island structures with very strong tunneling conductances were considered. Quantum fluctuations of the charge in the islands were found to renormalize all the characteristic quantities: the charging energies and tunneling couplings. As a result, the peaks observed in the linear conductance were found to shift and change in shape as the dimensionless tunneling conductances increase. Moreover, the peak heights were found to decrease logarithmically with decreasing temperature; this behaviour bears close resemblance to the multi-channel Kondo model.

In ultrasmall semiconductor quantum dots considered in Papers II-V, the level spacings were assumed so large that only one or at most two single-particle energy levels contribute to the electronic transport through the dots. A number of different configurations consisting of single and double quantum dots were considered. At low temperature, each one of them was found to exhibit Kondo-like resonances in the spectral functions (the density of states) and also in the differential conductance through the dot(s). The most important contributions of this part of the Thesis are the additional features arising from a second level in a single quantum dot and the Kondo physics in two capacitively coupled quantum dots.

The second part of the Thesis (Paper VI) elucidates the magnetization dynamics of Mn_{12}. The almost ideal crystalline structure of the experimental samples together with the coupling of the individual spins to lattice vibrations results to a set of intriguing phenomena. In particular, owing to thermally activated tunneling of single molecular spins a series of resonant peaks is revealed in the relaxation rates of magnetization. In this work, it was found that the tunneling at a given resonance may be enhanced or pinched off by a proper direction and magnitude of the external magnetic field. The main results of this part of the Thesis are concerned with the dynamic susceptibility which provides certain advantages over the conventional relaxation-rate measurements in studying thermally activated tunneling. In particular, the nonequilibrium and transient effects which sometimes plague other kinds of experiments are diminished due to the weakness of the ac excitation fields employed.

A third aspect emphasized throughout the Thesis is concerned with the development of a nonequilibrium transport theory applicable to all systems with a set of discrete

electronic or spin states coupled to bosonic and/or fermionic environments. The variety of systems and phenomena investigated in Papers I through VI serves as an ample test bed for various aspects of the theory, ranging from stationary nonequilibrium situations to transient phenomena.

In all the systems considered, one can identify one of the paradigms of quantum mechanics: a two-level system coupled to particle and/or heat reservoirs. Depending on the particular system, the two levels correspond to the following: the two lowest charge states in metal SED's; either the charge or the spin states in single quantum dots; the extended symmetric and antisymmetric superposition states in double quantum dots; and the tunneling-coupled degenerate ground states of a Mn_{12} spin. In all these models, also other states exist but only at higher energies. Hence at low enough temperatures, these may be neglected and we are left with an effective two-level system.

The interest in the two-level systems has recently been revived because of the thriving activity in the field of quantum computing. The key element in the notion of a quantum computer is the quantum bit, or qubit, which is just a coherent tunable two-level system. The main concerns for any realization of a qubit are the decoherence and quantum fluctuations induced by the surroundings of the system, and the actual presence of other states at higher energies. Further investigation of the SED and spin models introduced in this Thesis can provide invaluable information on the feasibility and limitations of the various proposed realizations of a qubit.

Finally, let us place this work into a broader scope by considering two strong trends in nanoelectronics. Firstly, the rapid progress of fabrication technologies towards cleaner materials and increasingly accurate patterning is likely to continue. Consequently, more and more of basic quantum-mechanical models are to be realized – many of which can be described within the theoretical framework developed in this Thesis. On the other hand, increasingly complex structures are being built and studied. On this front, the double-island and double-dot models investigated in this work may be seen as initial steps towards more complicated and larger scale applications.

References

[1] O. Brandt, L. Tapfer, R. Cingolani, K. Ploog, M. Hohenstein, and F. Phillipp, Phys. Rev. B **41**, 12599 (1990).

[2] L. Sohn, private communication, 2000.

[3] D. C. Ralph, C. T. Black, and M. Tinkham, Phys. Rev. Lett. **74**, 3241 (1995).

[4] C. T. Black, D. C. Ralph, and M. Tinkham, Phys. Rev. Lett. **76**, 688 (1996).

[5] D. C. Ralph, C. T. Black, and M. Tinkham, Phys. Rev. Lett. **78**, 4087 (1997).

[6] D. L. Klein, R. Roth, A. K. L. Lim, A. P. Alivisatos, and P. L. McEuen, Nature **389**, 699 (1997).

[7] C. Schönenberger, H. van Houten, and H. C. Donkersloot, Europhys. Lett. **20**, 249 (1992).

[8] D. Averin and K. Likharev, J. Low Temp. Phys. **62**, 345 (1986).

[9] T. Fulton and G. Dolan, Phys. Rev. Lett. **59**, 109 (1987).

[10] D. Averin and K. Likharev, in *Mesoscopic Phenomena in Solids*, edited by B. Altshuler, P. Lee, and R. Webb (Elsevier, Amsterdam, 1991).

[11] *Single Charge Tunneling*, Vol. B 294 of *NATO ASI Series*, edited by H. Grabert and M. Devoret (Plenum Press, New York, 1992).

[12] L. P. Kouwenhoven and P. L. McEuen, in *Nanotechnology*, edited by G. Timp (Springer, New York, 1999).

[13] S. Guéron, M. M. Deshmukh, E. B. Myers, and D. C. Ralph, Phys. Rev. Lett. **83**, 4148 (1999).

[14] A. Caneschi, D. Gatteschi, J. Laugier, P. Rey, R. Sessoli, and C. Zanchini, J. Am. Chem. Soc. **110**, 2795 (1988).

[15] D. Gatteschi, A. Caneschi, L. Pardi, and R. Sessoli, Science **265**, 1054 (1994).

[16] O. Kahn, *Molecular Magnetism* (VCH, New York, 1993).

[17] R. Sessoli, H. L. Tsai, A. R. Shake, S. Wang, J. B. Vincent, K. Folting, D. Gatteschi, G. Christou, and D. N. Hendrickson, J. Am. Chem. Soc. **115**, 1804 (1993).

[18] J. R. Friedman, M. P. Sarachik, J. Tejada, and R. Ziolo, Phys. Rev. Lett. **76**, 3830 (1996).

[19] J. M. Hernández, X. X. Zhang, F. Luis, J. Bartolomé, J. Tejada, and R. Ziolo, Europhys. Lett. **35**, 301 (1996).

[20] L. Thomas, F. Lionti, R. Ballou, D. Gatteschi, R. Sessoli, and B. Barbara, Nature **383**, 145 (1996).

[21] F. Luis, J. Bartolomé, and J. F. Fernández, Phys. Rev. B **57**, 505 (1998).

[22] H. Schoeller and G. Schön, Physica B **203**, 423 (1994).

[23] H. Schoeller and G. Schön, Phys. Rev. B **50**, 18436 (1994).

[24] J. König, H. Schoeller, and G. Schön, Europhys. Lett. **31**, 31 (1995).

[25] J. König, H. Schoeller, and G. Schön, in *Quantum Dynamics of Submicron Structures*, *NATO ASI, Series E*, edited by H. A. Cerdeira, B. Kramer, and G. Schön (Kluwer, Dordrecht, 1995).

[26] J. König, H. Schoeller, and G. Schön, Phys. Rev. Lett. **76**, 1715 (1996).

[27] J. König, J. Schmid, H. Schoeller, and G. Schön, Phys. Rev. B **54**, 16820 (1996).

[28] P. Lafarge, H. Pothier, E. R. Williams, D. Esteve, C. Urbina, and M. H. Devoret, Z. Phys. B **85**, 327 (1991).

[29] J. M. Martinis, M. Nahum, and H. D. Jensen, Phys. Rev. Lett. **72**, 904 (1994).

[30] E. H. Visscher, S. M. Verbrugh, J. Lindeman, P. Hadley, and J. E. Mooij, Appl. Phys. Lett. **66**, 305 (1994).

[31] F. R. Waugh, M. J. Berry, D. J. Mar, and R. M. Westervelt, Phys. Rev. Lett. **75**, 705 (1995).

[32] F. R. Waugh, M. J. Berry, C. H. Crouch, C. L. D. J. Mar, R. M. Westervelt, K. L. Campman, and A. C. Gossard, Phys. Rev. B **53**, 1413 (1996).

[33] L. W. Molenkamp, K. Flensberg, and M. Kemerink, Phys. Rev. Lett. **75**, 4282 (1995).

[34] K. A. Matveev, L. I. Glazman, and H. U. Baranger, Phys. Rev. B **53**, 1034 (1996).

[35] K. A. Matveev, L. I. Glazman, and H. U. Baranger, Phys. Rev. B **54**, 5637 (1996).

[36] J. M. Golden and B. I. Halperin, Phys. Rev. B **53**, 3893 (1996).

[37] J. M. Golden and B. I. Halperin, Phys. Rev. B **54**, 16757 (1996).

[38] J. M. Golden and B. I. Halperin, Phys. Rev. B **56**, 4716 (1997).

[39] N. Andrei, G. T. Zimányi, and G. Schön, Phys. Rev. B **60**, R5125 (1999).

[40] L. J. Geerlings, V. F. Anderegg, P. A. M. Holweg, J. E. Mooij, H. Pothier, D. Esteve, C. Urbina, and M. H. Devoret, Phys. Rev. Lett. **64**, 2691 (1990).

[41] K. K. Likharev, IEEE Trans. Magn. **23**, 1142 (1987).

[42] D. V. Averin and A. A. Odintsov, Phys. Lett. **40A**, 251 (1989).

[43] D. V. Averin and Y. V. Nazarov, Phys. Rev. Lett. **65**, 2446 (1990).

[44] D. V. Averin and Y. V. Nazarov, in *Single Charge Tunneling*, Vol. 294 of *NATO ASI, Series B*, edited by H. Grabert and M. Devoret (Plenum Press, New York, 1992), .

[45] J. König, H. Schoeller, and G. Schön, Phys. Rev. Lett. **78**, 4482 (1997).

[46] J. König, H. Schoeller, and G. Schön, Phys. Rev. B **58**, 7882 (1998).

[47] J. König, *Quantum Fluctuations in the Single-Electron Transistor* (Shaker, Aachen, 1999).

[48] P. Joyez, V. Bouchiat, D. Esteve, C. Urbina, and M. H. Devoret, Phys. Rev. Lett. **79**, 1349 (1997).

[49] K. A. Matveev, Zh. Eksp. Teor. Fiz. **99**, 1598 (1991), [Sov. Phys. JETP **72**, 892 (1991)].

[50] G. Falci, G. Schön, and G. T. Zimanyi, Phys. Rev. Lett. **74**, 3257 (1995).

[51] M. A. Kastner, Physics Today **46**, 24 (1993).

[52] L. Kouwenhoven, C. Marcus, P. McEuen, S. Tarucha, R. Westervelt, and N. Wingreen, in *Mesoscopic Electron Transport*, *NATO ASI, Series E*, edited by L. Sohn, L. P. Kouwenhoven, and G. Schön (Kluwer, Dordrecht, 1997).

[53] H. Schoeller, in *Mesoscopic Electron Transport*, *NATO ASI, Series E*, edited by L. Sohn, L. P. Kouwenhoven, and G. Schön (Kluwer, Dordrecht, 1997).

[54] B. S. V. J. Goldman and J. E. Cunningham, Science **255**, 313 (1992).

[55] P. Guéret, N. Blanc, R. Germann, and H. Rothuizen, Phys. Rev. Lett. **68**, 1896 (1992).

[56] R. Ashoori, H. L. Stormer, J. S. Weiner, L. N. Pfeiffer, S. J. Pearton, K. W. Baldwin, and K. W. West, Phys. Rev. Lett. **68**, 3088 (1992).

[57] A. T. Johnson, L. P. Kouwenhoven, W. de Jong, N. C. van der Vaart, C. J. P. M. Harmans, and C. T. Foxon, Phys. Rev. Lett **69**, 1592 (1992).

[58] J. Weis, R. J. Haug, K. v. Klitzing, and K. Ploog, Phys. Rev. B **46**, R12837 (1992).

[59] E. B. Foxman, P. L. McEuen, U. Meirav, N. S. Wingreen, Y. Meir, P. A. Belk, N. R. Belk, M. A. Kastner, and S. J. Wind, Phys. Rev. B **47**, R10020 (1993).

[60] S. Tarucha, D. G. Austing, and T. Honda, Superlattices and Microstructures **18**, 121 (1995).

[61] S. Tarucha, D.G.Austing, T. Honda, R. J. van der Hage, and L. Kouwenhoven, Phys. Rev. Lett. **77**, 3613 (1996).

[62] T. Schmidt, R. J. Haug, K. von Klitzing, A. Förster, and H. Lüth, Phys. Rev. Lett. **78**, 1544 (1997).

[63] P. W. Anderson, Phys. Rev. **124**, 41 (1961).

[64] C. W. J. Beenakker, Phys. Rev. B **44**, 1646 (1991).

[65] N. C. van der Vaart, S. F. Godijn, Y. V. Nazarov, C. J. P. M. Harmans, J. E. Mooij, L. W. Molenkamp, and C. T. Foxon, Phys. Rev. Lett. **74**, 4702 (1995).

[66] T. H. Oosterkamp, T. Fujisawa, W. G. van der Wiel, K. Ishibashi, R. V. Hijman, S. Tarucha, and L. P. Kouwenhoven, Nature **395**, 873 (1998).

[67] L. P. Kouwenhoven, N. C. van der Vaart, A. T. Johnson, W. Kool, C. J. P. M. Harmans, J. G. Williamson, A. A. M. Staring, and C. T. Foxon, Z. Phys. B **85**, 367 (1991).

[68] D. C. Ralph and R. A. Buhrman, Phys. Rev. Lett. **72**, 3401 (1994).

[69] R. H. Blick, J. Haug, J. Weis, D. Pfannkuche, K. v. Klitzing, and K. Eberl, Phys. Rev. B **53**, 7899 (1996).

[70] L. I. Glazman and M. E. Raikh, Pis'ma Zh. Eksp. Teor. Fiz. **47**, 378 (1988), [JETP Lett., **47**, 452 (1988)].

[71] T. K. Ng and P. A. Lee, Phys. Rev. Lett. **61**, 1768 (1988).

[72] S. Hershfield, J. H. Davies, and J. W. Wilkins, Phys. Rev. Lett. **67**, 3720 (1991).

[73] Y. Meir, N. S. Wingreen, and P. A. Lee, Phys. Rev. Lett. **66**, 3048 (1991).

[74] Y. Meir, N. S. Wingreen, and P. A. Lee, Phys. Rev. Lett. **70**, 2601 (1993).

[75] K. Flensberg, Phys. Rev. B **48**, 11156 (1993).

[76] K. A. Matveev, Phys. Rev. B **51**, 1743 (1995).

[77] A. Furusaki and K. A. Matveev, Phys. Rev. B **52**, 16676 (1995).

[78] D. Goldhaber-Gordon, J. Goeres, M. A. Kastner, H. Shtrikman, D. Mahalu, and U. Meirav, Phys. Rev. Lett. **81**, 5225 (1998).

[79] R. López, R. Aguado, G. Platero, and C. Tejedor, Phys. Rev. Lett. **81**, 4688 (1998).

[80] Y. Goldin and Y. Avishai, Phys. Rev. Lett. **81**, 5394 (1998).

[81] W. B. Thimm, J. Kroha, and J. von Delft, Phys. Rev. Lett. **82**, 2143 (1999).

[82] P. Nordlander, M. Pustilnik, Y. Meir, N. S. Wingreen, and D. C. Langreth, Phys. Rev. Lett. **83**, 808 (1999).

[83] A. Kaminski, Y. V. Nazarov, and L. I. Glazman, Phys. Rev. Lett. **83**, 384 (1999).

[84] A. L. Yeyati, F. Flores, and A. Martin-Rodero, Phys. Rev. Lett. **83**, 600 (1999).

[85] T. Pohjola, D. Boese, J. König, , H. Schoeller, and G. Schön, J. Low Temp. Phys. **118**, 391 (2000).

[86] U. Gerland, J. von Delft, T. A. Costi, and Y. Oreg, Phys. Rev. Lett. **84**, 3710 (2000).

[87] M. Eto and Y. V. Nazarov, Phys. Rev. Lett. **85**, 1306 (2000).

[88] A. L. Yeyati, A. Martin-Rodero, and F. Flores, Phys. Rev. Lett. **71**, 2991 (1993).

[89] Y. Meir and N. S. Wingreen, Phys. Rev. Lett. **68**, 2512 (1992).

[90] A. C. Hewson, *The Kondo Problem to Heavy Fermions* (Cambridge University Press, Cambridge, 1993).

[91] G. D. Mahan, *Many-Particle Physics* (Plenum Press, Dordrecht, 1990).

[92] M. Pustilnik, Y. Avishai, and K. Kikoin, Phys. Rev. Lett. **84**, 1756 (2000).

[93] M. Pustilnik and L. I. Glazman, Phys. Rev. Lett. **85**, 2993 (2000).

[94] U. Wilhelm and J. Weis, unpublished.

[95] U. Wilhelm and J. Weis, Physica E **6**, 668 (2000).

[96] J. Schmid, J. Weis, and K. Eberl, Physica E **6**, 375 (2000).

[97] J. Schmid, J. Weis, K. Eberl, and K. v. Klitzing, Phys. Rev. Lett. **84**, 5824 (2000).

[98] Sasaki, S. D. Franceschi, J. Elzerman, W. van der Wiel, M. Eto, S. Tarucha, and L. Kouwenhoven, Nature **405**, 764 (2000).

[99] D. Boese, W. Hofstetter, and H. Schoeller, unpublished.

[100] T. Ivanov, Europhys. Lett. **40**, 183 (1997).

[101] T. Ivanov, Phys. Rev. B **56**, 12339 (1997).

[102] T. Pohjola, J. König, M. Salomaa, J. Schmid, H. Schoeller, and G. Schön, Europhys. Lett. **40**, 189 (1997).

[103] W. Izumida, O. Sakai, and Y. Shimizu, J. Phys. Soc. Jpn. **66**, 717 (1997).

[104] W. Izumida, O. Sakai, and Y. Shimizu, J. Phys. Soc. Jpn. **67**, 2444 (1998).

[105] T. Aono, M. Eto, and K. Kawamura, J. Phys. Soc. Jpn. **67**, 1860 (1998).

[106] T. Aono and M. Eto, J. Low Temp. Phys. **118**, 401 (2000).

[107] J. M. Hernández, X. X. Zhang, F. Luis, J. Tejada, J. R. Friedman, M. P. Sarachik, and R. Ziolo, Phys. Rev. B **55**, 5858 (1997).

[108] F. Luis, J. Bartolomé, J. F. Fernández, J. Tejada, J. M. Hernández, X. X. Zhang, and R. Ziolo, Phys. Rev. B **55**, 11448 (1997).

[109] J. F. Fernández, F. Luis, and J. Bartolomé, Phys. Rev. Lett. **80**, 5659 (1998).

[110] J. R. Friedman, M. P. Sarachik, and R. Ziolo, Phys. Rev. B **58**, R14729 (1998).

[111] J. Villain, F. Hartmann-Boutron, R. Sessoli, and A. Rettori, Europhys. Lett. **27**, 159 (1994).

[112] P. Politi, A. Rettori, F. Hartmann-Boutron, and J. Villain, Phys. Rev. Lett. **75**, 537 (1995).

[113] F. Hartman-Boutron, P. Politi, and J. Villain, Int. J. Mod. Phys. B **10**, 2577 (1996).

[114] D. A. Garanin and E. M. Chudnovsky, Phys. Rev. B **56**, 11102 (1997).

[115] L. Gunther, Europhys. Lett. **39**, 1 (1997).

[116] A. Fort, A. Rettori, J. Villain, D. Gatteschi, and R. Sessoli, Phys. Rev. Lett. **80**, 612 (1998).

[117] N. V. Prokof'ev and P. C. E. Stamp, Phys. Rev. Lett. **80**, 5794 (1998).

[118] L. Thomas, A. Caneschi, and B. Barbara, Phys. Rev. Lett. **83**, 2398 (1999).

[119] M. N. Leuenberger and D. Loss, Europhys. Lett. **46**, 692 (1999).

[120] M. N. Leuenberger and D. Loss, Phys. Rev. B **61**, 1286 (2000).

[121] D. A. Garanin, E. M. Chudnovsky, and R. Schilling, Phys. Rev. B **61**, 12204 (2000).

[122] A. Caneschi, D. Gatteschi, and R.Sessoli, J. Am. Chem. Soc. **113**, 5873 (1991).

[123] R. Sessoli, D. Gatteschi, A. Caneschi, and M. A. Novak, Nature **365**, 141 (1993).

[124] M. Al-Saqer, V. V. Dobrovitski, B. N. Harmon, and M. I. Katsnelson, preprint cond-mat/9909278, 1999.

[125] I. Tupitsyn and B. Barbara, preprint cond-mat/0002180, 2000.

[126] T. Pohjola and H. Schoeller, Physica B **284-288**, 589 (2000).

[127] E. Chudnovsky and J. Tejada, *Macroscopic Quantum Tunneling of the Magnetic Moment* (Cambridge University Press, Cambridge, 1999).

[128] W. Wernsdorfer and R. Sessoli, Science **284**, 133 (1999).

[129] D. Loss, D. P. DiVincenzo, and G. Grinstein, Phys. Rev. Lett. **69**, 3232 (1992).

[130] J. von Delft and C. L. Henley, Phys. Rev. Lett. **69**, 3236 (1992).

[131] M. N. Leuenberger and D. Loss, preprint cond-mat/0006075, 2000.

[132] K. Blum, *Density Matrix Theory and Applications*, 2nd edition ed. (Plenum Press, New York, 1996).

[133] R. P. Feynman and F. L. Vernon, Ann. Phys. (N.Y.) **24**, 113 (1963).

[134] A. O. Caldeira and A. J. Leggett, Physica A **121**, 587 (1983).

[135] U. Weiss, *Quantum Dissipative Systems*, *Series in Modern Condensed Matter Physics* (World Scientific, Singapore, 1993).

[136] H. Schoeller, *Transport Theory of Interacting Quantum Dots*, 1997, Habilitationsschrift, Universität Karlsruhe.

[137] T. Pohjola and H. Schoeller, cond-mat/0005135, 2000.

[138] T. K. Ng, Phys. Rev. Lett. **76**, 487 (1996).

[139] H. Schoeller, in *Low-Dimensional Systems*, edited by T. Brandes (Springer, Hamburg, 2000).

[140] J. König and H. Schoeller, Phys. Rev. Lett. **81**, 3511 (1998).

[141] H. Schoeller and J. König, Phys. Rev. Lett. **84**, 3686 (2000).

Abstracts of Publications I-VI

I. We study the electron transport through a system of two low-capacitance metal islands connected in series between two electrodes. The work is motivated in part by experiments on semiconducting double-dots, which show intriguing effects arising from coherent tunneling of electrons and mixing of the single-electron states across tunneling barriers. In this article, we show how coherent tunneling affects metallic systems and leads to a mixing of the *macroscopic* charge states across the barriers. We apply a recently formulated RG approach to examine the linear response of the system with high tunnel conductances (up to $8e^2/h$). In addition we calculate the (second order) cotunneling contributions to the non-linear conductance. Our main results are that the peaks in the linear and nonlinear conductance as a function of the gate voltage are reduced and broadened in an asymmetric way, as well as shifted in their positions. In the limit where the two islands are coupled weakly to the electrodes, we compare to theoretical results obtained by Golden and Halperin and Matveev *et al.*. In the opposite case when the two islands are coupled more strongly to the leads than to each other, the peaks are found to shift, in qualitative agreement with the recent prediction of Andrei *et al.* for a similar double-dot system which exhibits a phase transition.

II. We study resonant tunneling through quantum-dot systems in the presence of strong Coulomb repulsion and coupling to the metallic leads. Motivated by recent experiments we concentrate on (i) a single dot with two energy levels and (ii) a double dot with one level in each dot. Each level is twofold spin-degenerate. Depending on the level spacing these systems are physical realizations of different Kondo-type models. Using a real-time diagrammatic formulation we evaluate the spectral density and the non-linear conductance. The latter shows a novel triple-peak resonant structure.

III. We study electron transport through single and double quantum dots with large level spacing and charging energy. Motivated by recent experiments we focus on linear and nonlinear response of two model systems: a single dot with two levels and a capacitively coupled double dot. At low temperature and strong coupling to the leads, quantum fluctuations and Kondo-like many-body effects become important and show up, e.g., as resonances in the current-voltage characteristics. In particular, we propose a way to observe the splitting of the Kondo peak as a function of the applied bias voltage.

IV. Motivated by recent experiments, we study electron transport through a system consisting of two ultrasmall capacitively-coupled quantum dots with a large level spacing and charging energy. At low temperature and strong coupling to the leads, quantum fluctuations of the charge and spin degrees of freedom strongly modify the conductance through the system and Kondo-like resonant effects arise. In this system, the Kondo effect has two possible origins, the spin and orbital degeneracies, and it is maximized when the two degeneracies occur simultaneously. Conductance is calculated for linear and nonlinear response and the temperature dependence of the resonant peak heights is quantified with poor man's scaling. For comparison, the cotunneling conductance in the Coulomb blockade regime is calculated.

V. Transport through quantum dots with large level spacing and charging energy is considered. At low temperature and strong coupling to the leads, quantum fluctuations and the Kondo effect become important. They show up, e.g., as zero-bias anomalies in the current-voltage characteristics. We use a recently developed diagrammatic technique as well as a new real-time renormalization-group approach to describe charge and spin fluctuations. Both approaches cover the linear as well as the nonlinear response regime. The spin fluctuations give rise to a Kondo-assisted enhancement of the current through the dot as seen in experiments.

VI. In this work, we study the spin dynamics of Mn_{12}-acetate molecules in the regime of thermally assisted tunneling. In particular, we describe the system in the presence of a strong transverse magnetic field. Similar to recent experiments, the relaxation time/rate is found to display a series of resonances; their Lorentzian shape is found to stem from the tunneling. The dynamic susceptibility $\chi(\omega)$ is calculated starting from the microscopic Hamiltonian and the resonant structure manifests itself also in $\chi(\omega)$. Similar to recent results reported on another molecular magnet, Fe_8, we find oscillations of the relaxation rate as a function of the transverse magnetic field when the field is directed along a hard axis of the molecules. This phenomenon is attributed to the interference of the geometrical or Berry phase. We propose susceptibility experiments to be carried out for strong transverse magnetic fields to study these oscillations and for a better resolution of the sharp satellite peaks in the relaxation rates.

ISBN 951-22-5324-0
ISSN 1456-3320